Materials Today Sustainability 28 (2024) 100988

Contents lists available at ScienceDirect

Materials Today Sustainability

journal homepage: www.journals.elsevier.com/materials-today-sustainability

Ab initio methods applied to carbon-containing defects in hexagonal boron nitride

Ao Wu [a,b], Danis I. Badrtdinov [c], Woncheol Lee [d], Malte Rösner [c], Cyrus E. Dreyer [e,f], Maciej Koperski [a,b,*]

[a] Department of Materials Science and Engineering, National University of Singapore, 117575, Singapore
[b] Institute for Functional Intelligent Materials, National University of Singapore, 117544, Singapore
[c] Radboud University, Institute for Molecules and Materials, Heijendaalseweg 135, 6525 AJ Nijmegen, Netherlands
[d] Materials Department, University of California, Santa Barbara, CA 93106-5050, USA
[e] Center for Computational Quantum Physics, Flatiron Institute, 162 5th Avenue, New York, NY 10010, USA
[f] Department of Physics and Astronomy, Stony Brook University, Stony Brook, New York 11794-3800, USA

ARTICLE INFO

Keywords:
Quantum defects
Ab initio methods
Density functional theory
Quantum embedding
Structural and electronic properties

ABSTRACT

The functionalities activated by defect centers in solids are constantly growing, opening new avenues for sustainable future technologies. These may extend to quantum optoelectronics if suitable defect centers are created and their properties understood. Recent progress in developing quantum emitters in hexagonal boron nitride (hBN) associated with carbon impurities enabled the realization of such concepts in atomically thin films, where the defect centers exhibit an unprecedented level of sensitivity toward the environment. The complexity of defects, together with new control knobs provided by van der Waals technology, poses a challenge for theory to accurately predict the properties of defect centers and to match them with experimental results. Here, we review the *ab initio* methods applied to carbon-containing defect centers in hBN, exploring the predictive capabilities of different levels of theory for their structural and optoelectronic properties.

1. Introduction

Since the discovery of graphene in 2004 [1,2], a tremendous number of atom-thick quantum materials have been fabricated. Among these, hexagonal boron nitride (hBN), a wide bandgap insulator with high thermal conductivity and chemical stability [3], has aroused great attention. The hBN surface is atomically smooth, free of dangling bonds and charge-trapping sites, with a honeycomb structure arising from sp^2 hybridization, similar to graphene. As a result, it serves as an excellent substrate for graphene and other two-dimensional (2D) materials. The atomically flat surface of hBN provides an ideal template for the epitaxial growth of 2D materials, resulting in minimal defects and controllable dielectric screening. This led to many improved properties, such as dramatically enhanced carrier mobility in graphene [4–6] or narrow excitonic resonances in transition metal dichalcogenide monolayers [7]. More recently, hBN demonstrated great potential in optoelectronic applications. The heteroatomic bonding of hBN leads to an optical band gap opened up to about 6 eV, making it an ideal deep UV emitter. Despite the indirect band nature [8], pure hBN shows strong luminescence in the deep UV range, achieved through the synthesis of high-purity hBN crystals in 2004 [9].

Besides pristine hBN, in recent years, impure hBN has emerged as a promising candidate in a range of quantum technologies, especially after the discovery of single photon emitters (SPEs) in hBN in 2016 across infrared (IR), visible, and ultraviolet (UV) spectral ranges [9–16]. This attracted significant attention because SPEs based on defects in other materials have been demonstrated as promising for quantum sensing [17–20], quantum nanophotonics [21–25], quantum information processing [26,27], and quantum communication [28,29]. Solid-state SPEs have been realized in diverse crystal structures, including the well-explored negatively charged nitrogen-vacancy (NV^{-1}) center in diamond [30–33], and various types of defects in silicon carbide (SiC) [34], ZnO [35], and transition metal dichalcogenides [36–38]. However, SPEs in 2D vdW hBN boast proximity to the dangling-bond-free, atomically flat surfaces, thus featuring (in principle) more stability and efficiency in quantum emission. In addition, these SPEs have been observed in diverse hBN samples, spanning single crystals [10,12], commercial powders [39], nanotubes [40], and epitaxial films [41–44]. The universality of robust color centers introduced in the numerous fabrication methods constitutes a challenge for the theoretical methods to assist in the identification of their atomic origin

* Corresponding author at: Institute for Functional Intelligent Materials, National University of Singapore, 117544, Singapore.
E-mail address: msemaci@nus.edu.sg (M. Koperski).

https://doi.org/10.1016/j.mtsust.2024.100988
Received 28 February 2024; Received in revised form 28 July 2024; Accepted 23 September 2024
Available online 30 September 2024

and comprehending the optoelectronic properties and their sensitivity to the environment at a microscopic level.

To better understand and control these SPEs in hBN, it is necessary to determine the microscopic structure and chemical nature of the color centers. This is a challenge in conventional semiconductors and has proved all the more challenging in hBN since the optical energies and lineshapes can vary over a wide range from sample to sample, and even between different locations in the sample sample [45]. For instance, the emission energies of the SPEs distribute mainly around 2.07 eV in the samples grown by molecular beam epitaxy (MBE) and chemical vapor deposition (CVD), while the emission energies span extensively from 1.55 to 2.50 eV in exfoliated films [39,41,42]. Also, as is the case with conventional semiconductors, *ab initio* theory [46,47] plays a key role in defect identification efforts. The phase space of possibilities is enormous, encompassing native imperfections like vacancies, interstitials, and antisites; impurity atoms; and complexes combining the two. Of these possibilities, carbon-containing defects have emerged as a possible source of SPEs, since C is a common impurity in hBN that can take on many forms [48–50]. Within this class of defects, there have been significant theoretical efforts to characterize and identify defects potentially present in hBN. In this review, we describe how state-of-the-art computational methods have significantly enhanced the understanding of potential C-based SPEs in hBN, and how such systems have been useful for benchmarking and comparing theoretical methods. This includes the electronic band structure, formation energy, and vibronic features at the density functional theory (DFT) level, and beyond-DFT techniques including GW calculations and quantum embedding methods. It should be noted that carbon-free defects are also likely the source of some of the well-known SPEs, though these are beyond the scope of this review. Other potential sources include oxygen/hydrogen-involved defects [51] and dangling bonds [52].

We begin by introducing the C-based defects we will discuss throughout (Section 2). Then, the remainder of this review is organized in terms of the *ab initio* methods used to tackle carbon-based defects in hBN, starting with DFT in Section 3, then GW and the Bethe–Salpeter equation (BSE) methods in Section 4, and finally quantum embedding methods in Section 5. In each section, we will give a brief overview of the general computational methodology, and then review its applications to carbon-based defects in hBN.

2. Carbon-based defect in hBN

Here we briefly introduce the general form of proposed C-based defects in hBN. The most commonly invoked motifs can be broken down into three categories [53–55], with some examples shown in Fig. 1. The simplest case results from isolated C impurities replacing B or N, *i.e.*, C_N [45,55–59] and C_B [45,55–58,60]. Also, it has been found that C impurities may form small clusters replacing several nearest-neighbor B and N atoms. Examples include the carbon dimer, C_BC_N [55,58], carbon trimers such as C_BC_2 and C_NC_2 [55,57,58,61,62], or even larger C clusters [55]. Finally, isolated C impurities or C impurity cluster may be adjacent to vacancies, *e.g.*, C_BV_N [55,59], C_NV_B [55,59], or $C_BC_NV_N$ [55].

3. Density function theory studies

Density functional theory (DFT) has been the workhorse for studying point defects for several decades [46,47], and the same is true for carbon-based defects in hBN. Some key defect properties from DFT are the formation energy, which gives their equilibrium concentration and therefore likelihood to form; the charge-state transition levels, which give the ionization energies and possible optical transitions; and the optical lineshapes of the defect, *i.e.*, the characteristic energy dependence of the luminescence/absorption spectra. In Section 3.1 we briefly describe the methodology for obtaining these properties and then their application to C-based defects in Section 3.2. Note that we do not attempt to provide a full review of DFT methods for defects, and instead focus on the quantities necessary to understand the relevant results for C-based defects in hBN. The reader is referred to Ref. [46] for a more complete discussion.

3.1. Methodology

3.1.1. Ground-state properties

The formation energy of a C-containing point defect in hBN, which determines its propensity to from, is given by [46]

$$\Delta H_f(D,q) = E_{\text{tot}}(D,q) - E_{\text{bulk}} - n_C\mu_C - n_B\mu_B - n_N\mu_N + q(E_v + E_F) + E_{\text{corr}} \quad (1)$$

where D denotes the defect, q is the charge state, $E_{\text{tot}}(D,q)$ is the energy of a supercell containing the defect, E_{bulk} is the corresponding energy of undefective hBN, n_i (μ_i) is the number (chemical potential) of atoms added or removed to create the defect (i = B, N, C), E_v is the valence band maximum (VBM) of hBN, E_F is the Fermi energy, and E_{corr} is a correction term for defect–defect interactions. $E_{\text{tot}}(D,q)$ and E_{bulk} are computed via DFT; the chemical potentials and Fermi level (with respect to the VBM) are inputs determined by the experimental situation.

For a given defect, the formation energy of the different charge states depends on the Fermi level, which can in principle range over the band gap of hBN. The positions in the band gap where the lowest energy charge state changes is referred to as the "thermodynamic charge-state transition energy". These energies play a key role, as they give the ionization energy with respect to the band edges. This is relevant for, *e.g.*, defect to band optical transitions. These should not be confused with neutral intra-defect excitations, where an electron is excited between defect levels.

3.1.2. Choice of exchange–correlation functional

The choice of exchange–correlation (XC) functional is key in DFT studies of defects in semiconductors and insulators. This is because accurate optical properties rely on an accurate treatment of the band gap, which is a consistent challenge for DFT. Replacing conventional local and semilocal functionals with hybrid functionals has emerged as a solution that balances accuracy and computational cost [46,47]. Even though Heyd–Scuseria–Ernzerhof [63] hybrid functional (HSE06) calculations of the hBN band gap give a closer estimation (5.7 eV) to the experimental value (6.1 eV) [8,64], a 30% average error about the band gap raises concerns on the capability to directly determine the transition energies. To solve this problem, more accurate *ab initio* methods are used [65]. In spite of that, direct assignment to the SPEs only focusing on the energy of the zero-phonon-lines (ZPLs) is questionable, with the ambiguity in the use of XC functionals. More details concerning the features of the PL spectrum have to be investigated thoroughly within a first-principle framework. These should include the position and lineshape of ZPL and phonon side band (PSB) peaks.

3.1.3. Optical properties and luminescence lineshapes

The defects in hBN have shown promising properties to act as SPEs, and thus it is crucial to understand their optical properties. In addition, the characteristic optical spectra of defects can serve as a "fingerprint" for defect identification. The basic properties of optical transitions can be understood via configuration-coordinate diagrams, as shown in Fig. 2(a). The parabolas correspond to potential energy surfaces of different electronic states. These can correspond to neutral intra-defect excitations, or defect to band transitions. They are displaced along the "configuration coordinate" axis, indicating that the two states have different atomic structures. The potential energy surfaces define vibrational wavefunctions, and optical transitions occur vertically between them (according to the Franck–Condon approximation) [66]. Assuming that we start from the ground vibrational state, the minimum

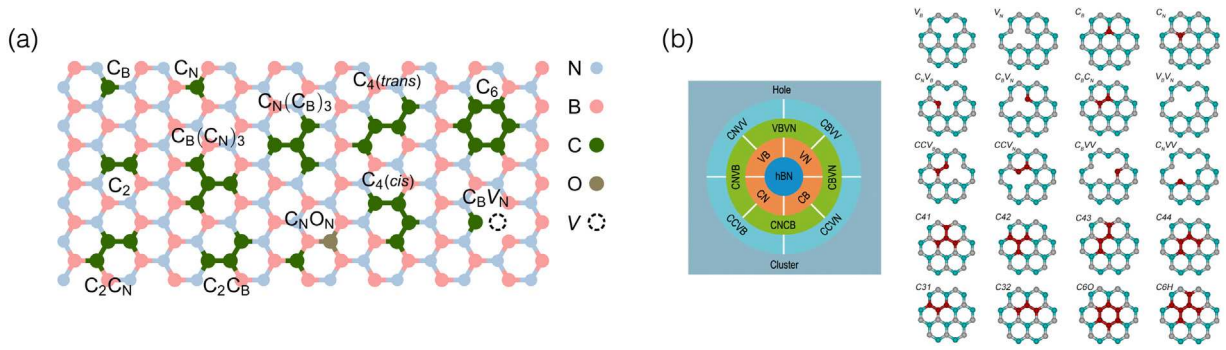

Fig. 1. Schematics of C-based defects in hexagonal BN. Panel (a) is adapted from Ref. [54], American Physical Society. Panel (b) is adapted from Ref. [55], American Physical Society.

(maximum) energy for absorption (luminescence) is called the zero-phonon line (ZPL); for all other transitions, the system ends up in an excited vibrational state, and this energy is dissipated via emission of phonons. This results in a phonon side band. The strength of the electron–phonon coupling, which is often parametrized via the Huang–Rhys factor [66], determines the relative weight of the spectra in the ZPL and the PSB [67]. For large Huang–Rhys factors, the spectra consist of a roughly Gaussian PSB, and the ZPL is not discernible, as in Fig. 2(b) for defects in GaN and ZnO [68]. For intermediate and small electron–phonon couplings, the ZPL is a relatively sharp peak, and the PSB has a characteristic structure, as in Fig. 2(c) for the NV^- center in diamond [69].

Since it has played such a significant role in understanding defects in hBN [56–58,70,71], we briefly review the state-of-the-are *ab initio* methodology for systematically modeling luminescence lineshape based on DFT calculations. The framework was first used on the luminescence of NV^- centers [69] and GaN [68], where luminescence lineshapes were reproduced in very good agreement with the experiment, as shown in Fig. 2(b,c). More information can be found in Refs. [47,69].

According to the Franck–Condon approximation, the transition dipole moment $\vec{\mu}_{eg}$ between the excited state and ground state is not affected by the change of ion coordinates. Fig. 2(a) gives the Huang–Rhys model of one-dimensional (1D) configuration coordinate for defect luminescence. The absolute luminescence intensity $I(\hbar\omega)$ is given by

$$I(\hbar\omega) = \frac{n\omega^3}{3\varepsilon_0\pi c^3\hbar}\left|\vec{\mu}_{eg}\right|^2 \times \sum_m \left|\left\langle \chi_{gm} \mid \chi_{e0}\right\rangle\right|^2 \delta\left(E_{ZPL} - E_{gm} - \hbar\omega\right). \tag{2}$$

Here, n is the refractive index of the material. $\langle \chi_{gm} \mid \chi_{e0}\rangle$ is the overlap integrals of the vibrational modes of excited and ground state, respectively. E_{gm} is the sum of the energy of all the χ_{gm} state with different wave vector k, *i.e.*, $E_{gm} = \sum_k n_k\hbar\omega_k$, n_k and ω_k the number and frequency of the phonons. It should be noted that the direct use of bulk modes (phonons of the pristine host) may not be accurate as lattice imperfections can introduce several local or quasi-local modes. To compare with the experiment, it is usually sufficient to compute the normalized luminescence intensity,

$$L(\hbar\omega) = C\omega^3 A(\hbar\omega), \tag{3}$$

with C the normalization constant $C^{-1} = \int A(\hbar\omega)\omega^3\,\mathrm{d}(\hbar\omega)$ and $A(\hbar\omega)$ the optical spectral function

$$A(\hbar\omega) = \sum_m \left|\left\langle \chi_{gm} \mid \chi_{e0}\right\rangle\right|^2 \delta\left(E_{ZPL} - E_{gm} - \hbar\omega\right). \tag{4}$$

The fundamental quantity that evaluates the coupling strength between electrons and phonons is the spectral function $S(\hbar\omega)$:

$$S(\hbar\omega) = \sum_k S_k \delta\left(\hbar\omega - \hbar\omega_k\right), \tag{5}$$

here S_k is defined as the partial Huang–Rhys (HR) factor for mode k with $S_k = \omega_k q_k^2/(2\hbar)$. q_k is given by

$$q_{\mathrm{k}} = \sum_{\alpha i} \sqrt{m_\alpha}\left(R_{\mathrm{e},\alpha i} - R_{\mathrm{g},\alpha i}\right) r_{\mathrm{k},\alpha i}, \tag{6}$$

where k, α, and i is the index for vibrational modes, atoms, and Cartesian coordinates $\{x, y, z\}$, respectively. R_e/R_g are the relaxed positions of atoms with mass m_α in the excited and ground states, respectively, and r_{k} is the normalized vector in the direction of normal mode k. In practice, the excited state atomic configuration is calculated through constrained DFT (cDFT) [72], where the occupation number is restricted, while the phonon normal modes are assumed to be identical after excitation.

Once $S(\hbar\omega)$ is determined, we can calculate the optical spectral function $A(\hbar\omega)$ through Fourier transformation of the generating function $G(t) = \mathrm{e}^{S(t)-S(0)}$, where $S(t)$ is the Fourier transformation of $S(\hbar\omega)$, yielding

$$A\left(E_{\mathrm{ZPL}} - \hbar\omega\right) = \frac{1}{2\pi}\int_{-\infty}^{\infty} G(t)\mathrm{e}^{i\omega t - \gamma|t|}\mathrm{d}t. \tag{7}$$

Here, γ corresponds to the broadening of the ZPL. We have written Eq. (7) such that the energy is normalized to the E_{ZPL}. This is because, due to the challenges of accurately determining the band gap mentioned in Section 3.1.2, the spectra are often slightly shifted to the proposed experimental ZPL energy. In addition, γ is also often taken from experiment, as it includes the combination of extrinsic inhomogeneous broadening and anharmonic phonon interactions, which are difficult to calculate *ab initio*. We note that the above methodology assumes that the normal modes of the excited state are identical to the ground state [69].

3.2. Application to C-containing defects in hBN

In this section, we review the application of the DFT methods described in the previous sections to C-based defects in hBN.

3.2.1. Formation energies

An exhaustive study of the thermodynamics of C-based defects was carried out by Maciaszek et al. [54]. The authors concluded that the "simpler" C-based defects, including C_B, C_N, and C_BC_N are more likely to be present in larger quantities. However, larger carbon clusters can be present under certain conditions in concentrations in excess of 10^{-14} cm^{-3}, and thus may still be observable SPEs. In terms of C atoms coupled to vacancies, they only found that C_BV_B was expected to be present in significant quantities. Notably, C_BV_N, which was proposed as the origin of the 1.6–2.1 eV SPE [73], was not expected to be a common impurity complex.

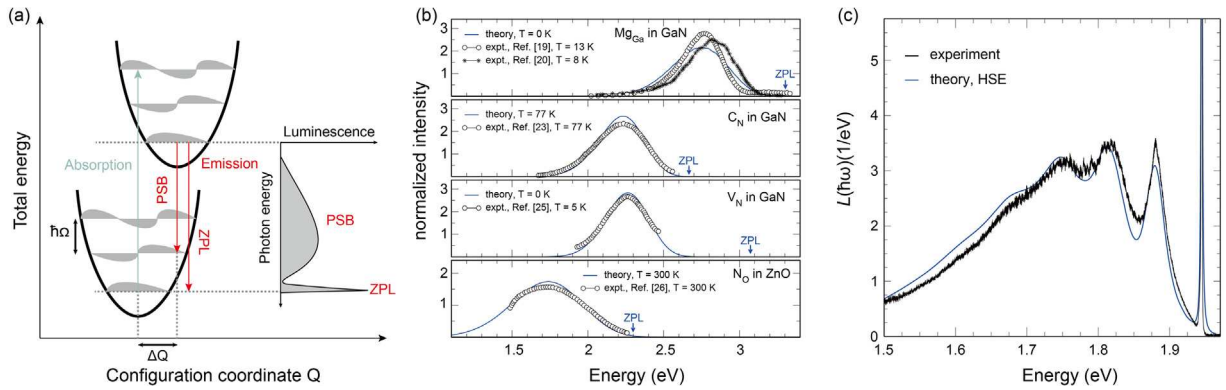

Fig. 2. (a) 1D configuration coordinate diagram for optical absorption and emission of point defects. Ω is the effective phonon frequency. ZPL and PSB refer to zero-phonon line and phonon sideband. The *ab initio* luminescence lineshape with comparison to experimental results is presented for (b) doped GaN/ZnO and (c) NV^- color center. Panel (b) is adapted from Ref. [68], American Physics Society. Panel (c) is adapted from Ref. [69], IOP Publishing Ltd and Deutsche Physikalische Gesellschaft.

3.2.2. Optical properties

Tawfik et al. [56], first utilized the above-mentioned framework in hBN SPEs and produced evidence that an experimentally observed SPE is related to C_BV_N defects. They first compared the luminescence lineshape. As is shown in Fig. 3(a), three featured phonon sideband peaks are identified within 20 meV energy shift to the experiment results, with similar intensity in regard to the normalized luminescence spectrum measured at 10 K [16]. They also evaluate the HR factor, partial HR factor S_k, and the spectral function of electron–phonon coupling $S(\hbar\omega)$, besides the PL lineshape. The HR factor is 1.66 for C_BV_N, almost like the value they calculated from the experimental PL lineshape. In addition, vibrational analysis shows that the phonon modes responsible for the PSB are rather nonlocal, which agrees well with the conclusion in Ref. [16]. However, the formation energy for C_BV_N is still high (8 eV for a neutral case), and whether it would appear in the experiment is therefore in question [74]. Nevertheless, this study demonstrates an excellent first principles computational workflow to be followed, with access to multiple properties, such as PL lineshape, HR factor, vibronic modes, etc. Although the framework is based on DFT with PBE functionals, which reduces the accuracy, it is still enough to capture the vibronic feature of the experimental PL lineshape. In addition, it was shown that the theoretical results considerably deviate from experiments when assuming the normal modes are the same in the ground and excited states. After employing the linear transformation approach of Duschinsky, the C_BV_N lineshape achieved an excellent agreement with the experiment, see Ref. [59] from the same group.

In the work of Grosso et al. [71], defect candidates including C_BV_N with singlet/triplet transitions (left/right panel of Fig. 3(b)) are studied. Though no evidence was found that the candidates are related to the SPEs observed in the experiment, the first principle study indicates that the significant geometry shift under excitation contributes to the strengthened emission via the PSB channels. The calculations of $S(\hbar\omega)$ highly resembled those from Ref. [56], both in singlet and triplet transition cases. With the previous statement that the defect is dominantly coupled with non-localized modes, this paper further emphasizes that the C_BV_N defects are dominantly coupled with low-energy acoustic phonons, again making the PSB identification at about 1.75 eV ambiguous [16].

In the work of Jara et al. [57], a prominent shift of the phonon side band around 160 meV was identified as a fingerprint, which is observed in most measurements [11,12,75,76]. The authors systematically calculated carbon-involved defects from monomers to trimers and also investigated double clusters when they are close enough to interact but not sufficiently close to form a larger cluster. They first confirmed that two neutral C trimers (C_BC_2 and C_NC_2) with ZPLs lying at 1.63 and 1.65 eV (utilizing hybrid HSE06 functionals) are most likely SPEs. We select the C_NC_2 case for demonstration in Fig. 3(c). These two clusters exhibit typical PSB replicas very close to experimental observations. The inset is taken from another work (Li et al. [62]) that yields very similar lineshape of C_NC_2 compared to Jara's. They also identify a radiative/nonradiative lifetime consistent with experimental results, together with a 2.13 eV ZPL energy produced from GW+BSE methods, consolidating the argument that C_NC_2 trimers are responsible for the well-known 2 eV emission. Similar to the C_NV_N cases, the significant bulk atom participation indicates a quasilocal feature in the electron–phonon coupling in the process of excitation, which results in a rather small HR factor. Back to Jara's work, in the research on double clusters, an interesting phenomenon is that ZPL energies decrease with increasing distance between two clusters. This can be attributed to narrowed transition gaps between levels due to reduced interactions between clusters. The finding indicates that the ZPLs are tunable. Although neutral C dimer's (C_BC_N) ZPL lies at 4.1 eV, far away from the near-infrared or visible spectral range, the PBS shift of 160 meV enables a C_B-C_N pair separated by more than one lattice site (or the so-called "donor–acceptor pair (DAP)") also to be a candidate for the SPEs in the visible or IR region. The same conclusion is drawn in the work of Anburger et al. [58] In addition, DFT calculations of defect formation energies also showed that the direct substitutive creation of C_BC_2 and C_NC_2 requires high energies, rendering a thermal formation mechanism unlikely. However, it is energetically more favorable to create them within hBN layer with vacancies already present.

Following the combined defect and PSB study of Refs. [56] and [71], in which only a subset of defects was considered, Ref. [70] represents a more thorough investigation, with carbon involved impurities and native defects in charged and neutral situations. They demonstrate that C_B, C_N and C_BC_N defects are the most fundamental elements in SPE constitution. The C_B, C_N, and C_BC_N dimer all produce similar PSB features, but the ZPL energies are quite different. Fig. 3(d) shows selected calculated PL lineshapes of the C_B and C_N defects as examples. After shifting the ZPL to the experimental value of 3.22 eV, the PSB replicas coincide with the experiment results, indicating C_B or C_N are responsible for the emitters found at 3.2 and 3.4 eV [77,78]. Furthermore, the C_BC_N luminescence can be modulated in terms of the DAP distance, similar to the statement in Ref. [57] as mentioned above, and in Ref. [58]. From the farthest to the nearest spaced DAPs, the C_B-C_N pairs produce narrow ZPL with a wide range of energies and with similar vibronic features, as is shown in Fig. 3(e), indicating a series of well-defined SPEs, though somehow not observed in previous experiments. For the low energy (1.6–2.3 eV) emitters, the results indicate that V_B and C DAPs at intermediate distances are the best candidates. In addition, we noted that the HSE functionals act nontrivially in determining the vibrational modes, compared to PBE functionals, for stiffening the interaction between atoms and contributing to a red shift of the well-known 160 meV PSB.

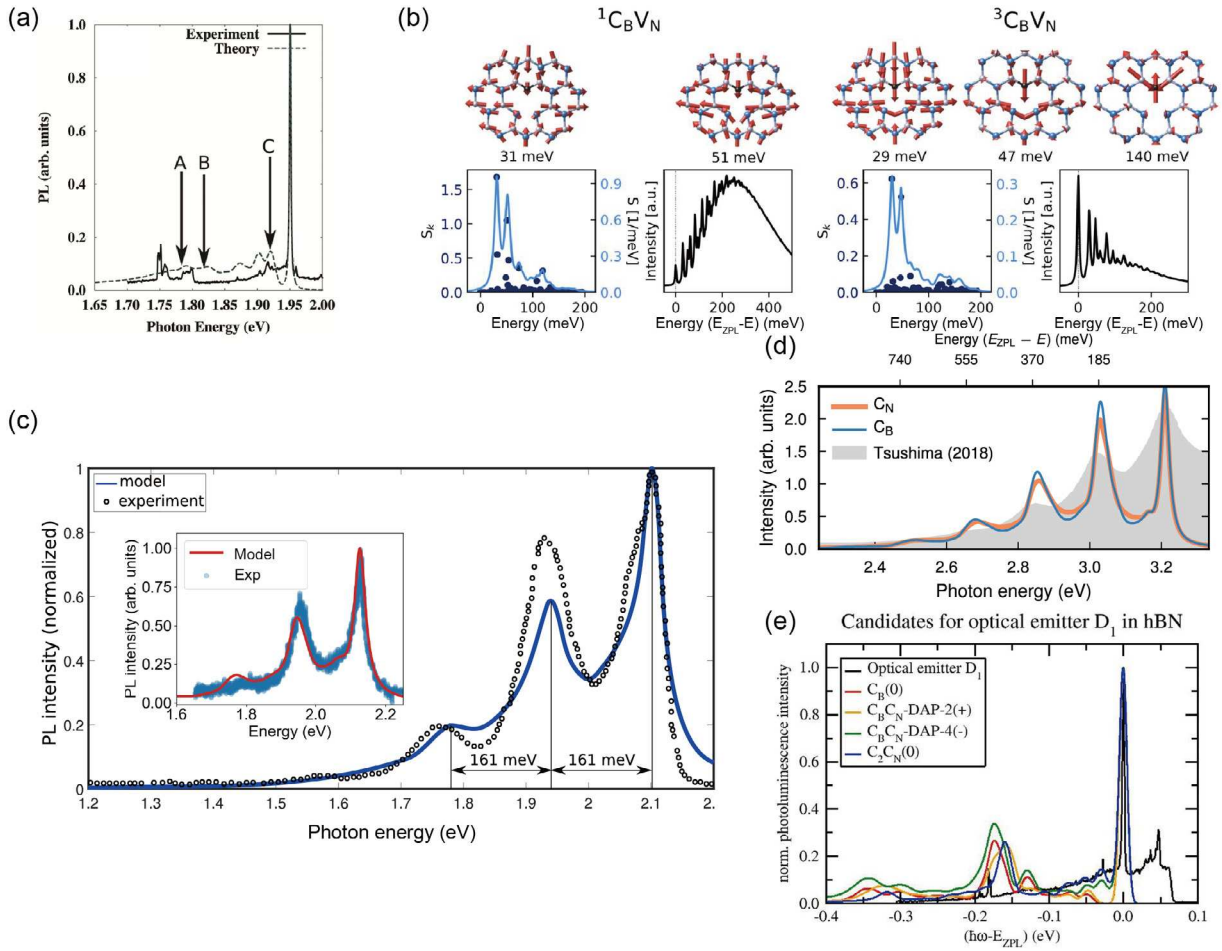

Fig. 3. The calculated PL lineshape based on the 1D configuration coordinate method from the first principle. (a) Theoretical PL lineshape of C_BV_N defects and comparison to experimental PL spectrum measured at 4 K, adapted from Ref. [56], The Royal Society of Chemistry. (b) Calculated partial Huang–Rhys factor S_k for phonon mode k and electron–phonon spectrum function, along with the theoretically predicted PSB relative to the ZPL for C_BV_N defects, adapted from Ref. [71], American Chemical Society. (c) Theoretical PL lineshape for neutral C_NC_2, with comparison to experimental emission around 2.0 eV [12], adapted from Ref. [57], American Chemical Society. The inset: result from Li et al. also regarding the C_NC_2 defects, adapted from Ref. [62], American Physical Society. (d) Calculated PL lineshape for neutral C_N and C_B compared with experimental results, adapted from Ref. [77], American Institute of Physics. The ZPL is shifted to the experimental value 3.22 eV. (e) Calculated PL lineshape for several candidates in neutral or charged state with comparison to the experimental result from Ref. [50], adapted from Ref. [70], American Physical Society.

4. *GW*-BSE theory

Within *ab initio GW* theory [79–84], the approximated exchange–correlation functional of DFT is replaced by a many-body self-energy, which is formally derived from a perturbation series around the screened Coulomb interaction. The result is a self-energy $\Sigma = iGW$ given by the product of the electronic propagator G (describing the electronic dispersion) and the screened Coulomb interaction W. This approach is especially appealing for gapped semiconductors as it can "heal" the strongly underestimated gap of (some flavors of) DFT and allows for a direct interpretation of the resulting spectral function as the energies needed to remove or add an electron to the system, which is strictly speaking not the case for the auxiliary single-particle Kohn–Sham eigenstates. Furthermore, it allows us to systematically account for the screening effects of the Coulomb interactions, which are naturally present in any realistic system. For layered van der Waals systems, this is especially important as screening is significantly suppressed in the monolayer limit and increases towards the bulk limit.

However, *GW* theory only allows the calculation of single-particle properties from first principles. Any estimates on optical properties based on this, *e.g.*, within Fermi's golden rule or the random-phase approximation, would only account for the re-normalized single-particle band gaps (or inter-impurity energies) and transition matrix elements as compared to DFT calculations. Especially for gapped systems, we know that these processes are not enough to describe optical gaps, as they neglect the formation of bound electron–hole states (excitons), which can form when electrons are optically excited from a valence to a conduction state. In fact, exciton absorption energies often lie in the single-particle gap and are thus responsible for a reduced optical gap. Since the binding between the electron and the hole forming the exciton is resulting from the screened Coulomb interaction, *GW* calculations and the description of the exciton properties are closely related. As we describe in more detail below, *GW* theory can be understood as the solution to the single-particle Dyson equation taking the screened Coulomb interaction to the lowest order into account. The corresponding description of two-particle processes, such as the formation of excitons, requires the solution of a two-particle Dyson equation, which is called the Bethe–Salpeter equation (BSE).

4.1. Methodology

The main approximation of *GW* theory is to neglect vertex corrections. By doing so, we can obtain the first (non-selfconsistent) corrections to the Kohn–Sham energies, by starting with calculating the bare (independent particle) polarization

$$\chi_0(1,2) = -iG_0(1,2)G_0(2,1)$$

using the "bare" (Kohn–Sham) Green's function G_0 and where numerical indices refer to combined position, time, and spin. With the polarization, we can evaluate the screened Coulomb interaction

$$W_0(1,2) = v(1,2) + \int v(1,3)\chi_0(3,4)W_0(4,2)d(3,4)$$

from the bare (unscreened) Coulomb interaction v, which can finally be used to calculate the G_0W_0 self-energy

$$\Sigma(1,2) = iG_0(1,2)W_0(1,2).$$

Linearizing the self-energy and focusing on diagonal elements only, we can approximately solve the Dyson equation, yielding G_0W_0 renormalized single-particle energies according to:

$$\varepsilon_k^{GW} = \varepsilon_k^{KS} + Z_k\langle\phi_k^{KS}|\Sigma_k(\varepsilon_k^{KS}) - V^{KS}|\phi_k^{KS}\rangle,$$

where Z_k is the quasi-particle weight and k is a combined momentum, band, and spin index. To describe two-particle (excitonic) properties, we write a Bethe–Salpeter equation (BSE) [81,85] for the four-point polarization

$$P(1,2,3,4) = P_0(1,2,3,4)+$$
$$\int P_0(1,2,5,6)K(5,6,7,8)P(7,8,3,4)d(5,6,7,8)$$

using the bare independent quasi-particle four point polarization $P_0(1,2,3,4) = -iG_0(1,3)G_0(2,4)$ and the four-point Coulomb kernel

$$K(1,2,3,4) = \delta_{12}\delta_{34}v(1,3) - \delta_{13}\delta_{24}W_0(1,2).$$

This BSE can be rewritten as a retarded Casida equation, which can be further approximated assuming statically screened Coulomb interactions only and applying the so-called Tamm–Dancoff approximation [85–87] yielding an effective two-particle Hamiltonian of the form

$$\left[(\varepsilon_c^{GW} - \varepsilon_v^{GW})\delta_{vv'}\delta_{cc'} + K_{vc,v'c'}\right]\Psi_x = \Omega_x\Psi_x \tag{8}$$

where v and c represent valence and conduction states (band, momentum, and spin indices). Diagonalizing this two-particle problem yields Ω_x, which represents single particle and excitonic excitation energies, and Ψ_x renders the corresponding oscillator strength. With these two quantities, one can construct an optical absorption spectrum including the effects of excitons.

4.2. Application

Ab initio GW calculations for pristine monolayer, few-layer, and bulk hBN have been performed regularly over the last three decades [91–96], which shows a common and expected trend: in comparison to conventional DFT calculations applying LDA/GGA functionals, the monolayer band gap (at K) increases by about 3 eV to 7.6–8.0 eV in G_0W_0 calculations, as depicted in Fig. 4(a). On the same level of GW theory, one further finds the total gap to be reduced by about 1 to 1.4 eV upon going from monolayer to bulk. Both of these trends, *i.e.*, from DFT to G_0W_0 and from monolayer to bulk (in G_0W_0), can be readily understood from the role of screened and non-local Coulomb interactions. In DFT (PBE) the effective Coulomb interaction is drastically "overscreened" (as LDA and GGA have been fitted to Quantum Monte Carlo (QMC) data for metals in which screening is strong), which is corrected in GW calculations. Thus, upon switching to GW calculations, the Coulomb interaction is more accurately described and handled (and especially its non-local tail), which is responsible for the drastic gap enhancement of about 3 eV. Increasing the number of layers from the monolayer case to the infinite stack of bulk increases the overall screening, which reduces the Coulomb interaction, such that the gap is reduced as well. These effects cannot be captured by conventional DFT calculations.

For the description of excitonic effects, GW-BSE calculations have been performed as well [88,89,97–100], yielding again a common trend: in the monolayer the optical gap including excitonic effects is reduced by about 2.0 eV to 5.3–6.0 eV. This reduction is, however, only present upon taking excitonic effects within the BSE approach into account, c.f. Fig. 4(b), and reflects the strong exciton binding energy of about 2.0 eV. This, in turn, is a direct measure of the strength of non-local Coulomb interaction in the system. At this stage, it is worth noting that there is a tendency towards cancellation effects in the excitonic absorption peak position from screening. That is, upon increasing screening both the band gap and the excitonic binding energies are possibly reduced to a similar extent, such that the excitonic absorption position in the optical spectrum can stay rather constant [97].

Since the *ab initio* description of defects requires supercell calculations with a significant amount of atoms/electrons, GW+BSE calculations for these cases have only become recently feasible. Examples range from single vacancies to single and double carbon substitutions and also more complex carbon-vacancy impurity structures [89,90,96,101–104]. On the single particle level, we find similar trends as for the hBN host itself: in GW gaps between occupied and unoccupied impurity states consequently widen with respect to conventional DFT calculations, c.f. Fig. 4(c,d). Additionally, the relative energetic positions to the hBN VBM and CBM are re-normalized as well. This, however, does not follow a generic trend but depends on the specific impurity.

For the *ab initio* calculation of optical spectra related to defects, we again need to differentiate between vertical excitations (which do not take any changes in the impurity configuration coordinate into account) and the ZPL energies, which include crystal structure changes upon charge neutral excitations. For the latter, we would in principle like to take GW (or RPA) corrected forces into account, which has to our knowledge, however, not been done yet. Instead, relaxations at constrained occupations within DFT are used to approximate the corresponding lattice deformations. In Fig. 4(e-h) we show a corresponding example for the C_BC_N carbon dimer [90]. Here the GdW (a variant of G_0W_0) widens the intra-impurity gap from 3.58 on the LDA level to 5.77 eV in GdW. Performing GdW+BSE calculations for both, the ground state lattice structures and the excited ones, yields a ZPL energy of 4.21 eV as depicted in Figs. 4(g,h), which is close to the experimental one around 4.1 eV. Additionally, there are several bright peaks between 5 and 6 eV. The one with the strongest oscillator strength mainly stems from transitions between the VBM and CBM and can be identified as the exciton of intrinsic hBN (close to the lowest exciton of GW calculations in pristine hBN).

Since the inter-impurity excitations are significantly controlled by the Coulomb interaction strength (within and between impurity related states), which in turn can be affected by screening from the surrounding, optical signals of the impurity states can change in energy when the environment is changed. As an approximately general trend, one can expect that increasing the environmental screening, *e.g.*, by changing from a monolayer to bulk or by exposing a monolayer to a dielectric substrate, decreases/redshifts impurity excitations [102,103,105]. However, also here there are counteracting trends at play which can yield to different or strongly reduced shifts depending on the impurity and the changes in the environment.

From this we conclude, that charged single- and charge-neutral two-particle excitations (such as excitons) can be described with modern *ab initio* GW+BSE approaches. These are capable of calculating intra-impurity excitations as well as those which take place between hBN host and impurity states. As a perturbative approach, GW+BSE can however not be applied for excitations within (or to/from) multi-reference states, which require a linear combination of Slater determinants to be described.

5. Quantum embedding methods

Another *ab initio* beyond-DFT methodology for treating defects is quantum embedding. In this section, we will introduce the general methodology, review its application to C-related defects in hBN, and discuss some key aspects of the methodology in the context of these types of defects.

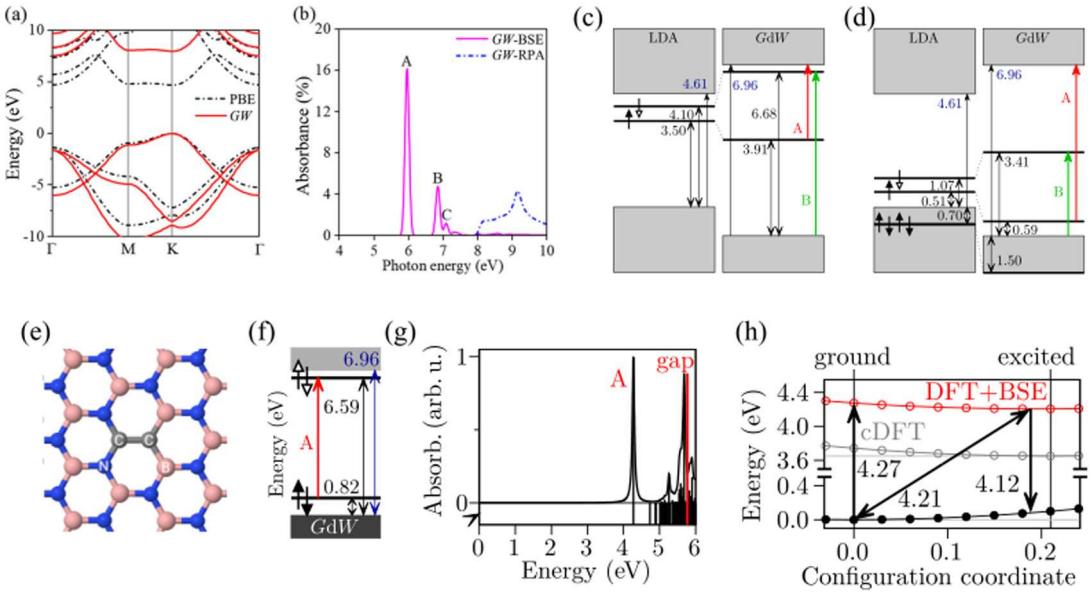

Fig. 4. (a) DFT-PBE (dashed black) and GW (solid red) band structures of pristine monolayer hBN. (b) Calculated absorption spectrum with (GW-BSE, solid pink) and without (GW-RPA, dash blue) electron–hole interactions for linearly polarized light. (c,d) Single-particle band-structure diagrams of C_B and C_N impurities in monolayer hBN. Small arrows pointing either up/down with filled/empty heads indicate the spin of an occupied/empty defect state. (e-h) Overview of the C_BC_N impurity. (e) Top view of the ground-state geometry. (f) Single-particle energy levels in GdW, showing one occupied defect state and one empty in-gap impurity state with a transition between them labeled "A". The resulting defect exciton is shown in (g) absorption spectrum at 4.27 eV, which is also the lowest exciton of the system. The peak at 5.6 eV resembles the lowest exciton of intrinsic hBN. (h) Total energies of the ground state (solid circles) and the excited state (open circles) as a function of the configuration coordinate. For the excited state, results from cDFT and GdW+BSE are shown. Panel (a,b) are adapted from Ref. [88], American Physical Society. Panel (c,d) are adapted from Ref. [89], American Physical Society. Panel (e-h) are adapted from Ref. [90], American Physical Society.

5.1. Methodology

Quantum embedding is a promising methodology that has emerged recently for describing properties of point defects that are challenging to capture with DFT, *e.g.*, excited states [106–108] or states that involve strong electron correlations [109,110]. The general idea is to treat a small part of the full electronic structure of a system with a many-body method, and the rest at a lower level of theory, *e.g.*, DFT [111,112]. Such approaches have enjoyed extensive success in quantum chemistry [112–128] and solid-state physics [111,129–131] for treating strongly correlated materials and molecules. They are ideal for treating defects since there is an intuitive definition of the active space, *i.e.*, the states associated with the defect, and often the host material, can accurately be treated via DFT, hybrid DFT, or GW. After this methodology was demonstrated for defects by Bockstedte et al. [132], it has rapidly increased in popularity [132–140].

The procedure for embedding begins with a DFT supercell calculation [46,141,142]. Then the active space of defect states (perhaps along with some other bulk states) are selected; the Hamiltonian in this space is

$$\begin{aligned} H = & -\sum_{ij,\sigma}(t_{ij}c^{\dagger}_{i\sigma}c_{j\sigma} + \text{H.c.}) \\ & + \frac{1}{2}\sum_{ijkl,\sigma\sigma'} U_{ijkl}c^{\dagger}_{i\sigma}c^{\dagger}_{j\sigma'}c_{l\sigma'}c_{k\sigma} \\ & - H_{\text{DC}} - \mu\sum_{i,\sigma} c^{\dagger}_{i\sigma}c_{i\sigma}, \end{aligned} \tag{9}$$

where σ,σ' indicate spin and i, j, k, l correspond to defect-related states (also referred to as the "active space"). Correspondingly, t_{ij} are the hopping matrix elements between active-space states, U_{ijkl} are the Coulomb matrix elements in the active space, screened by the rest of the states in the supercell, H_{DC} is a "double-counting" correction for the Coulomb interaction included in t_{ij} (Section 5.3.2), and μ is a chemical potential used to enforce the nominal occupation of the defect states.

The connection between the defect states and bulk is via the properties of the defect orbitals (which are informed by the symmetry of the crystal and hybridization with nearby atoms) and the screening of the Coulomb matrix elements. The Hamiltonian in Eq. (9) is then solved with a many-body method. In the next section, we review previous calculations using embedding methods for carbon-based defects in hBN; in Section 5.3 we discuss some important aspects of the methodology in the context of such defects.

5.2. Embedding applied to carbon defects in hBN

As mentioned above, the study of defects via quantum embedding is a relatively recent development; however, there already have been a handful of works so far applying quantum embedding to C-containing defects in hBN.

In Muechler et al. [138], the authors use the C_BC_N defect as a test case to explore different aspects of the embedding methodology. They derive all necessary matrix elements to define the Hamiltonian from Eq. (9) from first principles and solve it via exact diagonalization techniques. The physics of the many-body states could be understood by analogy to the Hubbard dimer. In terms of the quantitative properties, good agreement was found for the ZPL with the DFT calculations of Ref. [143], consistent with the 4.1 eV ZPL seen experimentally [144–146]. It was demonstrated that the DC correction was important for accurate results, and to remove the dependence on the choice of XC functional for the original DFT calculations (see Section 5.3.2).

Recent work by Lau et al. [139] also used C_BC_N as a test case to benchmark a somewhat different approach to defect quantum embedding. They begin from a Hartree–Fock description and do not perform any downfolding onto the active space, instead using the full unscreened Coulomb interaction. This requires a larger active space to include the relevant screening channels explicitly but is conceptually appealing since it avoids the need for a DC correction (see Section 5.3.2). Because of the larger active spaces, the many-body problem is solved via equation of motion coupled-cluster theory with singles and doubles [147–150]. The authors also demonstrate that by strategically choosing the basis orbitals and applying a composite correction via an additional configuration-interactions singles calculation,

they can achieve convergence with relatively few orbitals in the active space (order 10's instead of 100's). Their results for the singlet excitation energy are somewhat larger than found in Muechler et al. [138], but are in better agreement with the estimate of the experimental vertical excitation energy [102], demonstrating the promise of the methodology.

A more general set of defects in hBN was studied via quantum embedding in Ref. [105], including native defects and those containing C impurities. The goal of that work was to determine how defect properties changed with the environment of the defect, *e.g.*, whether it was located near the top of an hBN film or in the bulk. The embedding methodology, specifically the cRPA calculation of the screened Coulomb interaction, allowed for the quantification of the dielectric screening felt by the electrons in the defect orbitals. This showed that the dielectric environment played the most important role in changing the energies of the many-body states between a monolayer and bulk calculation.

In the work of Bhang et al., [140] first-principles methods including quantum embedding were used to propose a new class of defect complexes in hBN, which involve an impurity substituting on the N site bonded to an interstitial residing between the hBN layers, $X_N Y_i$ (X, Y = C, N, P, Si). These defects are interesting for quantum applications because they have the same point symmetry (C_{3v}) and NV^-, which is difficult to achieve for defect complexes restricted to the hBN planes. Remarkably, the ordering of the ground and excited many-body states (as determined by quantum embedding) is identical to that of NV^- ($^2A_2$, ^1E, ^1A, and ^3E), and the energies of these levels are even quantitatively similar. Thus the work of Ref. [140] is an excellent example of how first-principles calculations including many-body methods built on top of DFT can be used to predict novel C-containing quantum defects in hBN.

Though not specifically targeting C-containing defects, the work of Barcza et al. [136] is also a notable application of quantum embedding to defects in hBN. Those authors studied the negatively-charged boron vacancy via an embedding procedure that used a complete active space (CAS) protocol to select the active space, and density-matrix renormalization group (DMRG) to solve the many-body problem. DMRG allowed for a larger active space, and thus convergence with respect to active-space orbitals could be confirmed. Overall, this study demonstrated that quantum-chemistry-inspired embedding methods may be useful for defects in 2D materials.

5.3. Aspects of quantum embedding

5.3.1. Different roles of correlations for carbon defects

Let us discuss the different roles of correlations (via quantum embedding) realized on various types of carbon-based impurity complexes in hBN. As an example we consider carbon based C_BC_N, C_BV_N and $C_BC_NV_N$ defects [105]. Within DFT calculations all these defects form in-gap states (see Fig. 5), which were used as an active space. In the case of C_BC_N these states are formed by carbon-centered p_z-like orbitals hosting two electrons in total, while for C_BV_N two electrons reside on carbon-centered p_x-like orbital and two p_z-like empty orbitals, centered on C and at the neighboring B atoms. The $C_BC_NV_N$ can be interpreted as a combination of C_BC_N and C_BV_N orbitals with three electrons in total.

The level of correlation in these defects can be approximately quantified by the ratio of the single-particle hopping t between active orbitals and the effective local density–density U^* repulsion. In C_BC_N the hopping between two orbitals is $t \approx 1.32$ eV, while $U^* = 0.54$ eV, such that the ratio $t/U^* \sim 2.4$, which might be identified as weakly correlated here. As a result, we find the ground state of the C_BC_N impurity complex to be a singlet, which can be well described by mean-field theories, such as DFT. The first excited state is a triplet whose $m_s \pm 1$ state can also be described with a single Slater-determinant. The second charge neutral excitation is another singlet. The corresponding ZPL energy is close to the experimental 4.1 eV line [138]. For C_BV_N

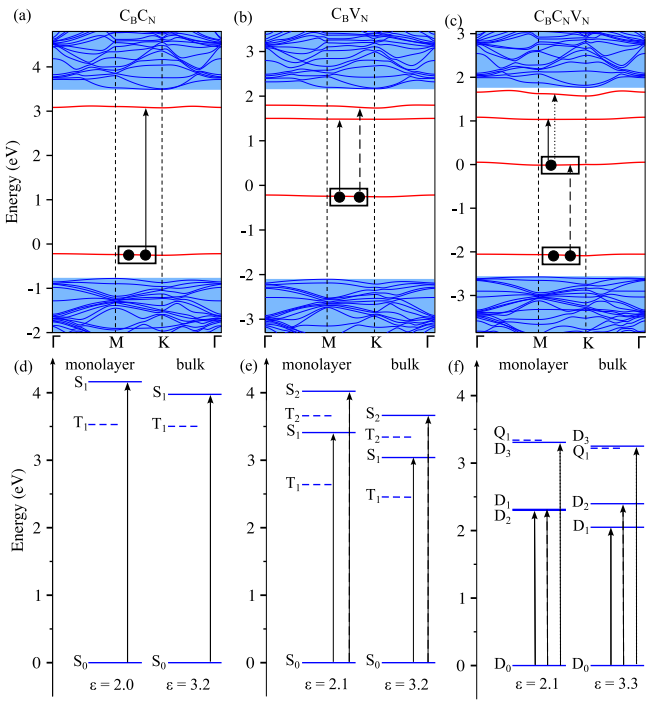

Fig. 5. (a-c) DFT band structures of considered carbon defects. Black dots sketch the initial occupations and their modification upon optical excitations. (d-f) Many-body impurity states for carbon defects in bulk and monolayer of hBN. Arrows demonstrate the possible excitations.
Source: The figure is adapted from Ref. [105], Wiley-VCH GmbH.

and $C_BC_NV_N$ the average hoppings ($\langle t \rangle = \frac{1}{N_{\text{orb}}} \sum_i |t_i|$) are approx. 0.53 eV and 0.43 eV, respectively. Together with the effective U^* = 0.94 eV and 0.72 eV, this suggests that also in these impurity complexes correlations play a moderate role. Nevertheless, in $C_BC_NV_N$ these embedding calculations predict the ground state to be a doublet, with various doublets and quadruplets as excitation energies. Since the Coulomb interactions are relevant for all excitation energies, changing the screening environment from monolayer to bulk hBN hosts decreases the excitations in most cases. The role of electron correlations may thus vary depending on the defect geometry and the involved active orbitals. Quantum embedding methods allow us to provide a detailed picture of these effects.

5.3.2. Double-counting approaches for defect embedding

As highlighted in the preceding section, the downfolding process and the accompanying challenge of double counting (DC) are pivotal factors influencing the accuracy of the embedding approach. Here we use the C_BC_N defect to perform a comparative analysis of approaches to DC that have been used in the defect literature. These include: the absence of a DC correction; a DC correction based on the assumption that DFT treats the Coulomb interaction in an analogous way as Hartree–Fock [132,134,135]; the use of G_0W_0 for a more rigorous treatment [151]; and the "dimer" DC correction [138], which was specifically tailored to C_BC_N.

We start out by noting that neglecting the DC correction for neutral intradefect excitation actually corresponds to the default assumption in the solid-state embedding community [129,152]. This is because an orbitally-averaged correction is the standard for, *e.g.*, dynamical mean-field theory calculations when downfolding from a DFT calculation; therefore the DC only changes the alignment between the active space bands and the uncorrelated electronic structure. This approach to DC would not change the intradefect transition energies, which have thus far been the focus of embedding studies. In any case, it has been

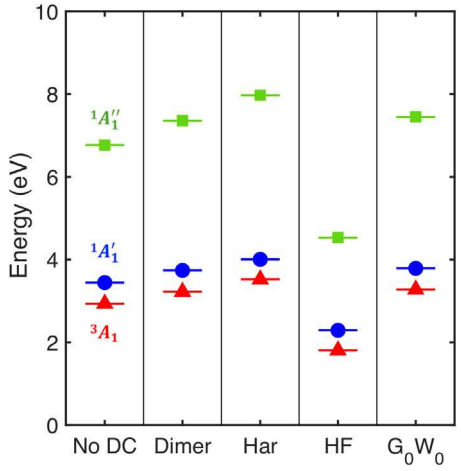

Fig. 6. Excited state energies of many-body states for C_BC_N in hBN, with respect to the ground-state singlet. Each column represents the result obtained with different DC corrections.
Source: The figure is adapted and expanded from Ref. [138], American Physical Society.

shown that an *orbitally selective* DC correction can be important in many systems to obtain accurate results [132,134,135,138,151].

The most common methodology so far [132,134,135,138] is to assume that the DFT treatment of the Coulomb interaction can be approximated to be related to that of Hartree–Fock. The general form of the DC contribution to the active-space Hamiltonian is

$$H_{\mathrm{DC}}^{\mathrm{hyb}} = \sum_{ij,\sigma} c_{i\sigma}^{\dagger} c_{j\sigma} \sum_{kl} \rho_{kl} \left(U_{iljk} - \alpha U_{ilkj} \right), \tag{10}$$

where ρ_{kl} is the component of the single-particle density matrix for orbitals k and l. If $\alpha = 1/2$, then Eq. (10) corresponds to the full Hartree–Fock treatment of the Coulomb interaction [153], except of course that U is screened by the states outside of the active space [134,135]. Often, if a hybrid functional is used for the original DFT calculation, α is set to the mixing parameter of the hybrid [132,138]; similarly, $\alpha = 0$ has been used when starting from local or semilocal functionals [138]. This approach operates under the approximation that the exchange–correlation part of the DC correction is expected to be less orbitally selective than the Hartree term [138,152].

The C_BC_N defect has a simple electronic structure and thus allows for a simple analysis of the DC correction. Based on the model of a Hubbard dimer [138], we expect six many-body states. The ground state is a singlet, which we denote as $^1A_1$, characterized by the presence of two electrons in the bonding b_2 orbital. Next, the first series of excited states constitutes a spin triplet manifold, indicated by $^3A_1$. This state results from the excitation of an electron from the b_2 orbital to the b_2^* orbital, with both electrons maintaining the same spin. Furthermore, an open-shell singlet state is identified, which we denote $^1A_1$, distinguished by the excitation of one electron possessing a spin opposite to that of the electron in the b_2 orbital. Lastly, there exists a second singlet state $^1A_1$, marked by the excitation of both electrons to the b_2^* orbital. Fig. 6 displays the results from an embedding calculation conducted with various DC schemes (performed on top of DFT calculations using the PBE [154] exchange–correlation potential). They all give precisely the sequence of many-body states predicted from the Hubbard dimer model.

The quantitative comparison between the dimer model and the many-body spectrum of C_BC_N allows us to construct a double-counting correction. From the methodologies outlined in Ref. [138] and derived from Ref. [155], the energies for the bonding and antibonding states can be expressed as $\epsilon_{b_2}^{DFT} = \epsilon_{b_2} + U_{b_2b_2b_2b_2}$ and $\epsilon_{b_2^*}^{DFT} = \epsilon_{b_2^*} + U_{b_2^*b_2b_2^*b_2}$, where ϵ^{DFT} indicates the DFT eigenvalue from a hypothetical exact exchange–correlation functional, and ϵ is the noninteracting energy. Therefore, eliminating the Coulomb interaction terms is equivalent to adjusting the single-particle energy levels. In this scenario, the intra-orbital interaction slightly exceeds the inter-orbital interaction, leading the DC correction to subtly increase the gap between the single-particle states. This correction, in turn, causes the many-body energy levels to shift upwards, as illustrated in the second column of Fig. 6. For the ideal Hubbard dimer and the exact DFT XC functional, the dimer DC is expected to be exact [155].

We now consider the Hartree ("Har") and Hartree–Fock ("HF") DC approaches. In the DFT ground state, on which the DC correction is based, C_BC_N exhibits only one non-zero occupation term ($\rho_{b_2b_2}$). This scenario results in the Hartree correction lowering the ground-state single-particle energy, thereby widening the gap to b_2^*. This increases the splittings of many-body states whose energies depend on the gap to b_2^* compared to the case where no DC correction is used (see Fig. 6). The gap between single-particle states becomes more pronounced than the adjustment seen with the dimer DC correction. The enhanced separation stems from the inclusion of extra non-zero components in addition to the density–density interaction terms ($U_{b_2b_2b_2b_2}$ and $U_{b_2^*b_2b_2^*b_2}$) incorporated in the dimer DC. Compared to the result without DC and with dimer DC, the application of Hartree DC results in higher many-body energies. However, we note that the accuracy of the Hartree double counting correction is compromised by the absence of the exchange–correlation double counting correction. Including the Fock exchange [$\alpha = 1/2$ in Eq. (10)] results in a significant reduction in the energies of the excited states due to the opposite sign of the exchange term. We expect that the full Fock exchange overestimates the orbital resolution of the true DFT XC potential, which is born out when we use the G_0W_0 approach to the DC.

The G_0W_0 approximation is widely recognized for its remarkable effectiveness in accurately determining quasiparticle energies across a diverse range of systems, including solids, molecules, and heterostructures [81,83,156]. Thus, employing G_0W_0 calculations as a low-level theory for describing the entire system presents a feasible approach. Moreover, it is reported that an exact double counting correction term can be derived within the G_0W_0 approximation [151]. We can express the formula for the double counting correction term within the G_0W_0 framework as

$$H_{\mathrm{DC}}^{G_0W_0} = V_{\mathrm{xc}} - iG_0W_0 + W_0^E \rho^A + iG_0^A W_0, \tag{11}$$

where the superscripts A and E indicate that the quantity is specified for the active space and the environment, respectively. The first two terms arise from the standard G_0W_0-level quasiparticle correction, as the one-body hopping matrix is obtained from DFT calculations. The third term is related to the Hartree correction previously mentioned, and the last term is the newly introduced term that corrects the double counting problem included the G_0W_0 calculation. Here G_0^A represents the Green's function for the active space, and W_0 denotes the Coulomb matrix that is screened by the entire system.

The last column of Fig. 6 displays the excitation energy derived from G_0W_0-level embedding calculations. Interestingly, there is a noticeable decrease in energies compared to the earlier mentioned Hartree correction. The energy reductions observed were 0.25 eV for the triplet state, 0.22 eV for the lowest singlet state, and a substantial decrease of 0.52 eV for the second singlet state. However, this reduction is significantly smaller than in the case of including the full Fock exchange. These findings underscore the need for a precise DC correction including the exchange–correlation interaction. It is also important to mention that the results from G_0W_0 DC are in close agreement with those obtained from the dimer DC. Specifically, for the singlet state, the excitation energy derived from the G_0W_0 embedding method was merely 50 meV greater than the result from the dimer DC correction. This supports the accuracy of the dimer model in describing the C_BC_N defect.

Table 1
Comparison between *ab initio* methods. Green check-marks indicate that a corresponding method had been applied to calculate a certain property for carbon-related impurities in hBN. The orange check-mark indicates that the corresponding property could be calculated, but has not. Optical properties are distinguished between excitations within impurity states and between impurity and host states. For the abbreviation definitions see footnotes below.

	Ground State			Excited State			Formation	Ionization	Vib.	Optical*		2D	Comp.
	Energy	Structure	Multiref.	Energy	Structure	Multiref.	Energy	Energy	Properties	Intra Imp.	Imp.-Host	Screening	Cost
DFT	✓	✓	✗	✗	✗	✗	✓	✓	✓	IPL	IPL	✗	low
cDFT / ΔSCF	✓	✓	✗	✓	✓	✗	✓	✓	✓	MF	MF	✗	low
GW	✓	(✓)[1]	✗	✓	✗	✗	(✓)	✓	(✓)	RPA	RPA	✓	medium
GW+BSE	✓	(✓)[1]	(✓)[2]	✓	✗	(✓)[3]	(✓)[1]	(✓)[1]	✗	BSE	BSE	✓	high
Embedding	✓	(✓)	✓	✓	✗	✓	(✓)	(✓)	✗	All	(All)	✓	medium

*: best possible
IPL: Independent Particle Level (no interactions)
RPA: Interactions handled on the Random Phase Approximation level
BSE: Bethe–Salpeter Equation (includes electron–hole interactions)
All: includes all interactions handled non-perturbatively
[1]: available on the RPA level
[2]: BSE corrections to QSGW exist [157]
[3]: BSE as single excitations.

6. Summary and outlook

Carbon-based defects in hBN result in a rich set of phenomena which clearly yield various opportunities for quantum defect engineering. However, it also constitutes a significant challenge in terms of defect identification and characterization. On the experimental side, there are significant differences in defect properties in different samples and even different locations in the same sample. On the theory side, there are many possible structures that give a wide range of observables. Identifying the microscopic origin of defects observed experimentally is a classic and enduring problem; the difference, in this case, is that the defects community now has a large and powerful toolkit of *ab initio* methods for calculating a larger variety of properties and obtaining accurate electronic structures.

In Table 1 we summarize the *ab initio* methods discussed in this review that have been applied to carbon-based defects in hBN. For these defects, DFT still plays the central role. Beyond its computation efficiency, this is because the defect structure and vibrational coupling to the host are crucial, and, at this point, there is no widespread alternative to DFT for a consistent treatment of such properties. In particular, the out-of-plane relaxations of some carbon-based defects can be rather large and different between different electronic states. Also, extending to constrained DFT allows geometry relaxation in excited states, which is needed for ZPL energies. The key limitation is that the excited state must be amenable to a single-determinant approximation; for more highly-correlated states, there is a strong need for many-body methods that can relax the geometry in the ground and excited electronic states [158].

In terms of optical properties, accurate results can be obtained with a variety of methods, ranging from hybrid-functionals (via ΔSCF), to *GW*+BSE, to quantum embedding. Each method has its strengths and weaknesses. The key advantage of DFT+ΔSCF is consistency in the treatment of atomic and electronic structure, though it is only possible in weakly correlated cases. Also, DFT makes qualitative errors in treating the dielectric screening in 2D, which has emerged as a crucial aspect in determining defect and bulk properties; indeed, accurately including screening on the defect properties in the presence of, *e.g.*, substrates, electrodes, or surfaces is an ongoing important development in the field. *GW* improves on this description of screening, treating it at the RPA level, and electron–hole interactions can be included via solutions to the BSE. Another advantage of these methods is that they improve the electronic structure of the defect as well as the hBN bulk host. For *GW*+BSE, however, this comes at a significant computational cost, which requires simplifying assumptions that depart slightly from the *ab initio* spirit. Furthermore, it is limited to states well-described within the space of single excitations. Quantum embedding solves some of these issues, allowing for highly correlated states at a (potentially) reduced computational cost due to downfolding to a smaller active space; the trade-off is an additional set of necessary assumptions/approximations. Combining *GW* with embedding, inspired by the correlated-materials community, has been shown to address some of these uncertainties (*e.g.*, the double-counting correction), and is overall a promising research direction.

Despite the complex interplay of advantages and limitations in the various methods brought to bear on carbon in hBN, there is a strikingly strong consensus between methods for some defects, *e.g.*, C_BC_N. This illustrates the power of multi-method studies to not only make confident predictions of defect properties but also learn about the accuracy or errors of the various methods; the variety of carbon-based defects in hBN, which have very different levels of correlation, make them an excellent test bed. Further, such studies are desired, with the goal of obtaining a better picture of which methods are appropriate for which defects, and for benchmarking additional capabilities developed for many-body methods (*e.g.*, forces). Finally, we note that *ab initio* many-body methods beyond perturbation theory, such as quantum Monte Carlo and coupled-cluster approximations, have been developed and implemented for defect systems. Despite their large computational cost, we believe that they have a role to play when it comes to benchmarking many-body perturbation theory and embedding approaches [159].

Overall, carbon-based defects in hBN are technologically exciting and tunable family for quantum applications, and an ideal testbed for benchmarking, comparing, developing, and utilizing state-of-the-art computational methods for treating defects. Recent experimental realizations of direct tunneling through defect centers in atomically thin hBN deposited on a graphite substrate unveil the mid-gap energy ladders, effects of electron–phonon coupling, and distinct geometries of the wavefunctions of electrons residing on the defect levels [160]. Global tunneling in vertical tunneling transistors enabled observation of electroluminescence [161] from carbon-doped hBN, while optically detected magnetic resonance studies [162] demonstrated the controllability of spin of individual defects. The next breakthroughs will likely originate by combining these methods, *e.g.*, by realizing scanning tunneling electroluminescence with coherent spin control. A deeper understanding of these phenomena will require the application of theoretical methods that appropriately account for the dominant interactions.

CRediT authorship contribution statement

Ao Wu: Writing – original draft, Software, Methodology, Investigation, Formal analysis. **Danis I. Badrtdinov:** Visualization, Software, Methodology, Investigation, Formal analysis. **Woncheol Lee:** Writing –

original draft, Software, Methodology, Investigation, Formal analysis, Data curation. **Malte Rösner:** Writing – review & editing, Writing – original draft, Validation, Supervision, Methodology, Investigation, Data curation, Conceptualization. **Cyrus E. Dreyer:** Writing – review & editing, Writing – original draft, Validation, Supervision, Software, Methodology, Investigation, Formal analysis, Data curation, Conceptualization. **Maciej Koperski:** Writing – review & editing, Writing – original draft, Supervision, Project administration, Funding acquisition, Conceptualization.

Declaration of competing interest

The authors declare that they have no known competing financial interests or personal relationships that could have appeared to influence the work reported in this paper.

Data availability

Data will be made available on request.

Acknowledgments

This project was supported by the Ministry of Education (Singapore) through the Research Centre of Excellence program (grant EDUN C-33-18-279-V12, I-FIM), AcRF Tier 3, Singapore (MOE2018-T3-1-005). This research is supported by the Ministry of Education, Singapore, under its Academic Research Fund Tier 2 (MOE-T2EP50122-0012). This material is based upon work supported by the Air Force Office of Scientific Research and the Office of Naval Research Global, United States under award number FA8655-21-1-7026. MR thanks the Simons Foundation for hospitality. CED acknowledges support from National Science Foundation, United States Grant No. DMR-2237674. The Flatiron Institute is a division of the Simons Foundation.

References

[1] K.S. Novoselov, A.K. Geim, S.V. Morozov, D. Jiang, Y. Zhang, S.V. Dubonos, I.V. Grigorieva, A.A. Firsov, Electric field effect in atomically thin carbon films, Science 306 (2004) 666.

[2] K.S. Novoselov, A.K. Geim, S.V. Morozov, D. Jiang, M.I. Katsnelson, I.V. Grigorieva, S.V. Dubonos, A.A. Firsov, Two-dimensional gas of massless dirac fermions in graphene, Nature 438 (2005) 197.

[3] M. Li, G. Huang, X. Chen, J. Yin, P. Zhang, Y. Yao, J. Shen, Y. Wu, J. Huang, Perspectives on environmental applications of hexagonal boron nitride nanomaterials, Nano Today 44 (2022) 101486.

[4] A.V. Kretinin, Y. Cao, J.S. Tu, G.L. Yu, R. Jalil, K.S. Novoselov, S.J. Haigh, A. Gholinia, A. Mishchenko, M. Lozada, T. Georgiou, C.R. Woods, F. Withers, P. Blake, G. Eda, A. Wirsig, C. Hucho, K. Watanabe, T. Taniguchi, A.K. Geim, R.V. Gorbachev, Electronic properties of graphene encapsulated with different two-dimensional atomic crystals, Nano Lett. 14 (2014) 3270.

[5] C.R. Dean, A.F. Young, I. Meric, C. Lee, L. Wang, S. Sorgenfrei, K. Watanabe, T. Taniguchi, P. Kim, K.L. Shepard, J. Hone, Boron nitride substrates for high-quality graphene electronics, Nat. Nanotechnol. 5 (2010) 722.

[6] A. Woessner, M.B. Lundeberg, Y. Gao, A. Principi, P. Alonso-González, M. Carrega, K. Watanabe, T. Taniguchi, G. Vignale, M. Polini, J. Hone, R. Hillenbrand, F.H.L. Koppens, Highly confined low-loss plasmons in graphene-boron nitride heterostructures, Nature Mater. 14 (2015) 421.

[7] W. Pacuski, M. Grzeszczyk, K. Nogajewski, A. Bogucki, K. Oreszczuk, J. Kucharek, K.E. Połczyńska, B. Seredyński, A. Rodek, R. Bozek, T. Taniguchi, K. Watanabe, S. Kret, J. Sadowski, T. Kazimierczuk, M. Potemski, P. Kossacki, Narrow excitonic lines and large-scale homogeneity of transition-metal dichalcogenide monolayers grown by molecular beam epitaxy on hexagonal boron nitride, Nano Lett. 20 (2020) 3058.

[8] G. Cassabois, P. Valvin, B. Gil, Hexagonal boron nitride is an indirect bandgap semiconductor, Nat. Photon. 10 (2016) 262.

[9] K. Watanabe, T. Taniguchi, H. Kanda, Direct-bandgap properties and evidence for ultraviolet lasing of hexagonal boron nitride single crystal, Nature Mater. 3 (2004) 404.

[10] T.T. Tran, K. Bray, M.J. Ford, M. Toth, I. Aharonovich, Quantum emission from hexagonal boron nitride monolayers, Nat. Nanotechnol. 11 (2016) 37.

[11] T.T. Tran, C. Elbadawi, D. Totonjian, C.J. Lobo, G. Grosso, H. Moon, D.R. Englund, M.J. Ford, I. Aharonovich, M. Toth, Robust multicolor single photon emission from point defects in hexagonal boron nitride, ACS Nano 10 (2016) 7331.

[12] L.J. Martínez, T. Pelini, V. Waselowski, J.R. Maze, B. Gil, G. Cassabois, V. Jacques, Efficient single photon emission from a high-purity hexagonal boron nitride crystal, PRB 94 (2016) 121405.

[13] A.L. Exarhos, D.A. Hopper, R.R. Grote, A. Alkauskas, L.C. Bassett, Optical signatures of quantum emitters in suspended hexagonal boron nitride, ACS Nano 11 (2017) 3328.

[14] N. Chejanovsky, M. Rezai, F. Paolucci, Y. Kim, T. Rendler, W. Rouabeh, F. Fávaro de Oliveira, P. Herlinger, A. Denisenko, S. Yang, I. Gerhardt, A. Finkler, J.H. Smet, J. Wrachtrup, Structural attributes and photodynamics of visible spectrum quantum emitters in hexagonal boron nitride, Nano Lett. 16 (2016) 7037.

[15] N.R. Jungwirth, G.D. Fuchs, Optical absorption and emission mechanisms of single defects in hexagonal boron nitride, PRL 119 (2017) 057401.

[16] T.Q.P. Vuong, G. Cassabois, P. Valvin, A. Ouerghi, Y. Chassagneux, C. Voisin, B. Gil, Phonon-photon mapping in a color center in hexagonal boron nitride, PRL 117 (2016) 097402.

[17] S. Lee, J.-S. Yeo, Y. Ji, C. Cho, D.-Y. Kim, S.-I. Na, B.H. Lee, T. Lee, Flexible organic solar cells composed of P3HT:PCBM using chemically doped graphene electrodes, Nanotechnology 23 (2012) 344013.

[18] A. Abderrahmane, P.J. Ko, T.V. Thu, S. Ishizawa, T. Takamura, A. Sandhu, High photosensitivity few-layered $MoSe_2$ back-gated field-effect phototransistors, Nanotechnology 25 (2014) 365202.

[19] X. Li, J. Yin, J. Zhou, W. Guo, Large area hexagonal boron nitride monolayer as efficient atomically thick insulating coating against friction and oxidation, Nanotechnology 25 (2014) 105701.

[20] M. Abdi, P. Degenfeld-Schonburg, M. Sameti, C. Navarrete-Benlloch, M.J. Hartmann, Dissipative optomechanical preparation of macroscopic quantum superposition states, PRL 116 (2016) 233604.

[21] F. Xia, H. Wang, D. Xiao, M. Dubey, A. Ramasubramaniam, Two-dimensional material nanophotonics, Nat. Photon. 8 (2014) 899.

[22] G. Clark, J.R. Schaibley, J. Ross, T. Taniguchi, K. Watanabe, J.R. Hendrickson, S. Mou, W. Yao, X. Xu, Single defect light-emitting diode in a Van der Waals heterostructure, Nano Lett. 16 (2016) 3944.

[23] R.-J. Shiue, D.K. Efetov, G. Grosso, C. Peng, K.C. Fong, D. Englund, Active 2D materials for on-chip nanophotonics and quantum optics, Nanophotonics 6 (2017) 1329.

[24] A.F. Koenderink, A. Alù, A. Polman, Nanophotonics: Shrinking light-based technology, Science 348 (2015) 516.

[25] J.D. Caldwell, I. Aharonovich, G. Cassabois, J.H. Edgar, B. Gil, D.N. Basov, Photonics with hexagonal boron nitride, Nat. Rev. Mater. 4 (2019) 552.

[26] J. Cai, A. Retzker, F. Jelezko, M.B. Plenio, A large-scale quantum simulator on a diamond surface at room temperature, Nat. Phys. 9 (2013) 168.

[27] J.J. Pla, K.Y. Tan, J.P. Dehollain, W.H. Lim, J.J.L. Morton, D.N. Jamieson, A.S. Dzurak, A. Morello, A single-atom electron spin qubit in silicon, Nature 489 (2012) 541.

[28] V. Scarani, H. Bechmann-Pasquinucci, N.J. Cerf, M. Dušek, N. Lütkenhaus, M. Peev, The security of practical quantum key distribution, RMP 81 (2009) 1301.

[29] H.-K. Lo, M. Curty, K. Tamaki, Secure quantum key distribution, Nat. Photon. 8 (2014) 595.

[30] I. Aharonovich, E. Neu, Diamond nanophotonics, Adv. Opt. Mater. 2 (2014) 911.

[31] J.R. Maze, A. Gali, E. Togan, Y. Chu, A. Trifonov, E. Kaxiras, M.D. Lukin, Properties of nitrogen-vacancy centers in diamond: The group theoretic approach, New J. Phys. 13 (2011) 025025.

[32] A. Gali, M. Fyta, E. Kaxiras, *Ab initio* supercell calculations on nitrogen-vacancy center in diamond: Electronic structure and hyperfine tensors, Phys. Rev. B 77 (2008) 155206.

[33] M.W. Doherty, N.B. Manson, P. Delaney, L.C.L. Hollenberg, The negatively charged nitrogen-vacancy centre in diamond: The electronic solution, New J. Phys. 13 (2011) 025019.

[34] A. Lohrmann, B.C. Johnson, J.C. McCallum, S. Castelletto, A review on single photon sources in silicon carbide, Rep. Progr. Phys. 80 (2017) 034502.

[35] A.J. Morfa, B.C. Gibson, M. Karg, T.J. Karle, A.D. Greentree, P. Mulvaney, S. Tomljenovic-Hanic, Single-photon emission and quantum characterization of zinc oxide defects, Nano Lett. 12 (2012) 949.

[36] M. Koperski, K. Nogajewski, A. Arora, V. Cherkez, P. Mallet, J.-Y. Veuillen, J. Marcus, P. Kossacki, M. Potemski, Single photon emitters in exfoliated WSe_2 structures, Nat. Nanotechnol. 10 (2015) 503.

[37] M. Koperski, M.R. Molas, A. Arora, K. Nogajewski, A.O. Slobodeniuk, C. Faugeras, M. Potemski, Optical properties of atomically thin transition metal dichalcogenides: Observations and puzzles, Nanophotonics 6 (2017) 1289.

[38] J. Howarth, K. Vaklinova, M. Grzeszczyk, G. Baldi, L. Hague, M. Potemski, K.S. Novoselov, A. Kozikov, M. Koperski, Electroluminescent vertical tunneling junctions based on WSe_2 monolayer quantum emitter arrays: Exploring tunability with electric and magnetic fields, Proc. Natl. Acad. Sci. 121 (2024) e2401757121.

[39] M. Koperski, K. Nogajewski, M. Potemski, Single photon emitters in boron nitride: More than a supplementary material, Opt. Commun. 411 (2018) 158.

[40] N. Chejanovsky, Y. Kim, A. Zappe, B. Stuhlhofer, T. Taniguchi, K. Watanabe, D. Dasari, A. Finkler, J.H. Smet, J. Wrachtrup, Quantum light in curved low dimensional hexagonal boron nitride systems, Sci. Rep. 7 (2017) 14758.

[41] A. Hernández-Mínguez, J. Lähnemann, S. Nakhaie, J.M.J. Lopes, P.V. Santos, Luminescent defects in a few-layer *h*-BN film grown by molecular beam epitaxy, Phys. Rev. Applied 10 (2018) 044031.

[42] N. Mendelson, Z.-Q. Xu, T.T. Tran, M. Kianinia, C. Bradac, J. Scott, M. Nguyen, J. Bishop, J. Froch, B. Regan, I. Aharonovich, M. Toth, Bottom up engineering of near-identical quantum emitters in atomically thin materials, 2018, arXiv: 1806.01199 [physics.app-ph].

[43] H.L. Stern, R. Wang, Y. Fan, R. Mizuta, J.C. Stewart, L.-M. Needham, T.D. Roberts, R. Wai, N.S. Ginsberg, D. Klenerman, S. Hofmann, S.F. Lee, Spectrally resolved photodynamics of individual emitters in large-area monolayers of hexagonal boron nitride, ACS Nano 13 (2019) 4538.

[44] M. Koperski, K. Pakula, K. Nogajewski, A.K. Dabrowska, M. Tokarczyk, T. Pelini, J. Binder, T. Fas, J. Suffczynski, R. Stepniewski, A. Wysmolek, M. Potemski, Towards practical applications of quantum emitters in boron nitride, Sci. Rep. 11 (2021) 15506.

[45] F. Hayee, L. Yu, J.L. Zhang, C.J. Ciccarino, M. Nguyen, A.F. Marshall, I. Aharonovich, J. Vučković, P. Narang, T.F. Heinz, J.A. Dionne, Revealing multiple classes of stable quantum emitters in hexagonal boron nitride with correlated optical and electron microscopy, Nature Mater. 19 (2020) 534.

[46] C. Freysoldt, B. Grabowski, T. Hickel, J. Neugebauer, G. Kresse, A. Janotti, C.G. Van de Walle, First-principles calculations for point defects in solids, Rev. Modern Phys. 86 (2014) 253.

[47] C.E. Dreyer, A. Alkauskas, J.L. Lyons, A. Janotti, C.G. Van de Walle, First-principles calculations of point defects for quantum technologies, Ann. Rev. Mater. Res. 48 (2018) 1.

[48] M. Koperski, D. Vaclavkova, K. Watanabe, T. Taniguchi, K.S. Novoselov, M. Potemski, Midgap radiative centers in carbon-enriched hexagonal boron nitride, Proc. Natl. Acad. Sci. 117 (2020) 13214.

[49] N. Mendelson, D. Chugh, J.R. Reimers, T.S. Cheng, A. Gottscholl, H. Long, C.J. Mellor, A. Zettl, V. Dyakonov, P.H. Beton, S.V. Novikov, C. Jagadish, H.H. Tan, M.J. Ford, M. Toth, C. Bradac, I. Aharonovich, Identifying carbon as the source of visible single-photon emission from hexagonal boron nitride, Nature Mater. 20 (2021) 321.

[50] N. Chejanovsky, A. Mukherjee, J. Geng, Y.-C. Chen, Y. Kim, A. Denisenko, A. Finkler, T. Taniguchi, K. Watanabe, D.B.R. Dasari, P. Auburger, A. Gali, J.H. Smet, J. Wrachtrup, Single-spin resonance in a Van der Waals embedded paramagnetic defect, Nat. Mater. 20 (2021) 1079.

[51] L. Weston, D. Wickramaratne, M. Mackoit, A. Alkauskas, C.G. Van de Walle, Native point defects and impurities in hexagonal boron nitride, PRB 97 (2018) 214104.

[52] M.E. Turiansky, A. Alkauskas, L.C. Bassett, C.G. Van de Walle, Dangling bonds in hexagonal boron nitride as single-photon emitters, PRL 123 (2019) 127401.

[53] W. Liu, N.-J. Guo, S. Yu, Y. Meng, Z.-P. Li, Y.-Z. Yang, Z.-A. Wang, X.-D. Zeng, L.-K. Xie, Q. Li, J.-F. Wang, J.-S. Xu, Y.-T. Wang, J.-S. Tang, C.-F. Li, G.-C. Guo, Spin-active defects in hexagonal boron nitride, Mater. Quantum Technol. 2 (2022) 032002.

[54] M. Maciaszek, L. Razinkovas, A. Alkauskas, Thermodynamics of carbon point defects in hexagonal boron nitride, Phys. Rev. Mater. 6 (2022) 014005.

[55] P. Huang, M. Grzeszczyk, K. Vaklinova, K. Watanabe, T. Taniguchi, K.S. Novoselov, M. Koperski, Carbon and vacancy centers in hexagonal boron nitride, Phys. Rev. B 106 (2022) 014107.

[56] S.A. Tawfik, S. Ali, M. Fronzi, M. Kianinia, T.T. Tran, C. Stampfl, I. Aharonovich, M. Toth, M. Ford, First principles investigation of quantum emission from hBN defects, Nanoscale (2017).

[57] C. Jara, T. Rauch, S. Botti, M.A.L. Marques, A. Norambuena, R. Coto, J.E. Castellanos-Águila, J.R. Maze, F. Munoz, First-principles identification of single photon emitters based on carbon clusters in hexagonal boron nitride, J. Phys. Chem. A 125 (2021) 1325.

[58] P. Auburger, A. Gali, Towards ab initio identification of paramagnetic substitutional carbon defects in hexagonal boron nitride acting as quantum bits, PRB 104 (2021) 075410.

[59] A. Sajid, J.R. Reimers, M.J. Ford, Defect states in hexagonal boron nitride: Assignments of observed properties and prediction of properties relevant to quantum computation, PRB 97 (2018) 064101.

[60] F. Wu, A. Galatas, R. Sundararaman, D. Rocca, Y. Ping, First-principles engineering of charged defects for two-dimensional quantum technologies, Phys. Rev. Materials 1 (2017) 071001.

[61] O. Golami, K. Sharman, R. Ghobadi, S.C. Wein, H. Zadeh-Haghighi, C. Gomes da Rocha, D.R. Salahub, C. Simon, Ab initio and group theoretical study of properties of a carbon trimer defect in hexagonal boron nitride, PRB 105 (2022) 184101.

[62] K. Li, T.J. Smart, Y. Ping, Carbon trimer as a 2 eV single-photon emitter candidate in hexagonal boron nitride: A first-principles study, Phys. Rev. Materials 6 (2022) L042201.

[63] J. Heyd, G.E. Scuseria, M. Ernzerhof, Hybrid functionals based on a screened coulomb potential, J. Chem. Phys. 118 (2003) 8207.

[64] C. Elias, P. Valvin, T. Pelini, A. Summerfield, C.J. Mellor, T.S. Cheng, L. Eaves, C.T. Foxon, P.H. Beton, S.V. Novikov, B. Gil, G. Cassabois, Direct band-gap crossover in epitaxial monolayer boron nitride, Nature Commun. 10 (2019) 2639.

[65] J.R. Reimers, A. Sajid, R. Kobayashi, M.J. Ford, Understanding and calibrating density-functional-theory calculations describing the energy and spectroscopy of defect sites in hexagonal boron nitride, J. Chem. Theory Comput. 14 (2018) 1602.

[66] A.M. Stoneham, Theory of Defects in Solids: Electronic Structure of Defects in Insulators and Semiconductors, Oxford University Press, Oxford, UK, 2001.

[67] A. Alkauskas, M.D. McCluskey, C.G. Van de Walle, Tutorial: Defects in semiconductors—combining experiment and theory, J. Appl. Phys. 119 (2016) 181101.

[68] A. Alkauskas, J.L. Lyons, D. Steiauf, C.G. Van de Walle, First-principles calculations of luminescence spectrum line shapes for defects in semiconductors: The example of GaN and ZnO, PRL 109 (2012) 267401.

[69] A. Alkauskas, B.B. Buckley, D.D. Awschalom, C.G. Van de Walle, First-principles theory of the luminescence lineshape for the triplet transition in diamond NV centres, New J. Phys. 16 (2014) 073026.

[70] C. Linderälv, W. Wieczorek, P. Erhart, Vibrational signatures for the identification of single-photon emitters in hexagonal boron nitride, PRB 103 (2021) 115421.

[71] G. Grosso, H. Moon, C.J. Ciccarino, J. Flick, N. Mendelson, L. Mennel, M. Toth, I. Aharonovich, P. Narang, D.R. Englund, Low-temperature electron–phonon interaction of quantum emitters in hexagonal boron nitride, ACS Photon. 7 (2020) 1410.

[72] A. Hellman, B. Razaznejad, B.I. Lundqvist, Potential-energy surfaces for excited states in extended systems, J. Chem. Phys. 120 (2004) 4593.

[73] A. Sajid, K.S. Thygesen, V_NC_B defect as source of single photon emission from hexagonal boron nitride, 2D Mater. 7 (2020) 031007.

[74] S. Li, A. Gali, Bistable carbon-vacancy defects in h-BN, Front. Quantum Sci. Technol. 1 (2022) 1007756.

[75] D. Wigger, R. Schmidt, O. Del Pozo-Zamudio, J.A. Preuß, P. Tonndorf, R. Schneider, P. Steeger, J. Kern, Y. Khodaei, J. Sperling, S.M. de Vasconcellos, R. Bratschitsch, T. Kuhn, Phonon-assisted emission and absorption of individual color centers in hexagonal boron nitride, 2D Mater. 6 (2019) 035006.

[76] A.V. Gritsienko, A. Duleba, M.V. Pugachev, N.S. Kurochkin, I.I. Vlasov, A.G. Vitukhnovsky, A.Y. Kuntsevich, Photodynamics of bright subnanosecond emission from pure single-photon sources in hexagonal boron nitride, 2022.

[77] E. Tsushima, T. Tsujimura, T. Uchino, Enhancement of the deep-level emission and its chemical origin in hexagonal boron nitride, Appl. Phys. Lett. 113 (2018) 031903.

[78] B. Berzina, V. Korsaks, L. Trinkler, A. Sarakovskis, J. Grube, S. Bellucci, Defect-induced blue luminescence of hexagonal boron nitride, Diam. Relat. Mater. 68 (2016) 131.

[79] L. Hedin, New method for calculating the one-particle Green's function with application to the electron-gas problem, Phys. Rev. 139 (1965) A796.

[80] F. Aryasetiawan, O. Gunnarsson, The GW method, Rep. Progr. Phys. 61 (1998) 237.

[81] G. Onida, L. Reining, A. Rubio, Electronic excitations: Density-functional versus many-body Green's-function approaches, Rev. Modern Phys. 74 (2002) 601.

[82] K. Held, C. Taranto, G. Rohringer, A. Toschi, Hedin equations, GW, GW+DMFT, and all that, https://arxiv.org/abs/1109.3972 [cond-mat], 1109.3972 [cond-mat].

[83] L. Reining, The GW approximation: content, successes and limitations, WIREs Comput. Mol. Sci. 8 (2018) e1344.

[84] D. Golze, M. Dvorak, P. Rinke, The GW compendium: A practical guide to theoretical photoemission spectroscopy, Front. Chem. 7 (2019).

[85] T. Sander, E. Maggio, G. Kresse, Beyond the Tamm-Dancoff approximation for extended systems using exact diagonalization, Phys. Rev. B 92 (2015) 045209.

[86] P.-F. Loos, P. Romaniello, Static and dynamic Bethe–Salpeter equations in the T-matrix approximation, J. Chem. Phys. 156 (2022) 164101.

[87] M. Huix-Rotllant, B. Natarajan, A. Ipatov, C.M. Wawire, T. Deutsch, M.E. Casida, Assessment of noncollinear spin-flip Tamm–Dancoff approximation time-dependent density-functional theory for the photochemical ring-opening of oxirane, Phys. Chem. Chem. Phys. 12 (2010) 12811.

[88] F. Zhang, C.S. Ong, J.W. Ruan, M. Wu, X.Q. Shi, Z.K. Tang, S.G. Louie, Intervalley excitonic hybridization, optical selection rules, and imperfect circular dichroism in monolayer h-BN, Phys. Rev. Lett. 128 (2022) 047402.

[89] A. Kirchhoff, T. Deilmann, P. Krüger, M. Rohlfing, Electronic and optical properties of a hexagonal boron nitride monolayer in its pristine form and with point defects from first principles, Phys. Rev. B 106 (2022) 045118.

[90] A. Kirchhoff, T. Deilmann, M. Rohlfing, Excited-state geometry relaxation of point defects in monolayer hexagonal boron nitride, Phys. Rev. B 109 (2024) 085127.

[91] X. Blase, A. Rubio, S.G. Louie, M.L. Cohen, Quasiparticle band structure of bulk hexagonal boron nitride and related systems, Phys. Rev. B 51 (1995) 6868.

[92] H. Şahin, S. Cahangirov, M. Topsakal, E. Bekaroglu, E. Akturk, R.T. Senger, S. Ciraci, Monolayer honeycomb structures of group-IV elements and III-V binary compounds: First-principles calculations, Phys. Rev. B 80 (2009) 155453.

[93] N. Berseneva, A. Gulans, A.V. Krasheninnikov, R.M. Nieminen, Electronic structure of boron nitride sheets doped with carbon from first-principles calculations, Phys. Rev. B 87 (2013) 035404.

[94] Q. Fu, D. Nabok, C. Draxl, Energy-level alignment at the interface of graphene fluoride and boron nitride monolayers: An investigation by many-body perturbation theory, J. Phys. Chem. C 120 (2016) 11671.

[95] F.A. Rasmussen, P.S. Schmidt, K.T. Winther, K.S. Thygesen, Efficient many-body calculations for two-dimensional materials using exact limits for the screened potential: Band gaps of MoS_2, hBN, and phosphorene, Phys. Rev. B 94 (2016) 155406.

[96] D. Wang, R. Sundararaman, Layer dependence of defect charge transition levels in two-dimensional materials, Phys. Rev. B 101 (2020) 054103.

[97] L. Wirtz, A. Marini, A. Rubio, Excitons in boron nitride nanotubes: Dimensionality effects, Phys. Rev. Lett. 96 (2006) 126104.

[98] F. Ferreira, A.J. Chaves, N.M.R. Peres, R.M. Ribeiro, Excitons in hexagonal boron nitride single-layer: A new platform for polaritonics in the ultraviolet, J. Opt. Soc. Am. B, JOSAB 36 (2019) 674.

[99] R.J. Hunt, B. Monserrat, V. Zólyomi, N.D. Drummond, Diffusion quantum Monte Carlo and GW study of the electronic properties of monolayer and bulk hexagonal boron nitride, Phys. Rev. B 101 (2020) 205115.

[100] L. Artús, M. Feneberg, C. Attaccalite, J.H. Edgar, J. Li, R. Goldhahn, R. Cuscó, Ellipsometry study of hexagonal boron nitride using synchrotron radiation: Transparency window in the far-UVC, Adv. Photon. Res. 2 (2021) 2000101.

[101] F. Wu, A. Galatas, R. Sundararaman, D. Rocca, Y. Ping, First-principles engineering of charged defects for two-dimensional quantum technologies, Phys. Rev. Mater. 1 (2017) 071001.

[102] M. Winter, M.H.E. Bousquet, D. Jacquemin, I. Duchemin, X. Blase, Photoluminescent properties of the carbon-dimer defect in hexagonal boron-nitride: A many-body finite-size cluster approach, Phys. Rev. Mater. 5 (2021) 095201.

[103] S. Zhang, K. Li, C. Guo, Y. Ping, Effect of environmental screening and strain on optoelectronic properties of two-dimensional quantum defects, 2D Mater. 10 (2023) 035036.

[104] D. Zhong, S. Gao, M. Saccone, J.R. Greer, M. Bernardi, S. Nadj-Perge, A. Faraon, Carbon-related quantum emitter in hexagonal boron nitride with homogeneous energy and 3-fold polarization, Nano Lett. 24 (2024) 1106.

[105] D.I. Badrtdinov, C. Rodriguez-Fernandez, M. Grzeszczyk, Z. Qiu, K. Vaklinova, P. Huang, A. Hampel, K. Watanabe, T. Taniguchi, L. Jiong, M. Potemski, C.E. Dreyer, M. Koperski, M. Rösner, Dielectric environment sensitivity of carbon centers in hexagonal boron nitride, Small 19 (2023) 2300144.

[106] W. Kohn, L.J. Sham, Self-consistent equations including exchange and correlation effects, Phys. Rev. 140 (1965) A1133.

[107] J.P. Perdew, A. Zunger, Self-interaction correction to density-functional approximations for many-electron systems, Phys. Rev. B 23 (1981) 5048.

[108] P. Mori-Sánchez, A.J. Cohen, W. Yang, Localization and delocalization errors in density functional theory and implications for band-gap prediction, Phys. Rev. Lett. 100 (2008) 146401.

[109] U. von Barth, Local-density theory of multiplet structure, Phys. Rev. A 20 (1979) 1693.

[110] J. Lischner, J. Deslippe, M. Jain, S.G. Louie, First-principles calculations of quasiparticle excitations of open-shell condensed matter systems, Phys. Rev. Lett. 109 (2012) 036406.

[111] Q. Sun, G.K.-L. Chan, Quantum embedding theories, Acc. Chem. Res. 49 (2016) 2705.

[112] L.O. Jones, M.A. Mosquera, G.C. Schatz, M.A. Ratner, Embedding methods for quantum chemistry: Applications from materials to life sciences, J. Am. Chem. Soc. 142 (2020) 3281.

[113] J.L. Pascual, L. Seijo, Z. Barandiarán, Ab initio model potential study of the optical absorption spectrum of Mn^{2+}-doped CaF_2, J. Chem. Phys. 103 (1995) 4841.

[114] R. Llusar, M. Casarrubios, Z. Barandiarán, L. Seijo, Ab initio model potential calculations on the electronic spectrum of Ni_2^+-doped MgO including correlation, spin–orbit and embedding effects, J. Chem. Phys..

[115] T. Klüner, N. Govind, Y.A. Wang, E.A. Carter, Periodic density functional embedding theory for complete active space self-consistent field and configuration interaction calculations: Ground and excited states, J. Chem. Phys. 116 (2002) 42.

[116] D. Muñoz Ramo, J.L. Gavartin, A.L. Shluger, G. Bersuker, Spectroscopic properties of oxygen vacancies in monoclinic HfO_2 calculated with periodic and embedded cluster density functional theory, Phys. Rev. B 75 (2007) 205336.

[117] A.S.P. Gomes, C.R. Jacob, L. Visscher, Calculation of local excitations in large systems by embedding wave-function theory in density-functional theory, Phys. Chem. Chem. Phys. 10 (2008) 5353.

[118] B. Swerts, L.F. Chibotaru, R. Lindh, L. Seijo, Z. Barandiaran, S. Clima, K. Pierloot, M.F.A. Hendrickx, Embedding fragment ab initio model potentials in CASSCF/CASPT2 calculations of doped solids: Implementation and applications, J. Chem. Theory Comput. 4 (2008) 586.

[119] B. Swerts, L.F. Chibotaru, R. Lindh, L. Seijo, Z. Barandiaran, S. Clima, K. Pierloot, M.F.A. Hendrickx, Embedding fragment ab initio model potentials in CASSCF/CASPT2 calculations of doped solids: Implementation and applications, J. Chem. Theory Comput. 4 (2008) 586.

[120] P. Huang, E.A. Carter, Advances in correlated electronic structure methods for solids, surfaces, and nanostructures, Annu. Rev. Phys. Chem. 59 (2008) 261.

[121] J.L. Pascual, N. Barros, Z. Barandiarán, L. Seijo, Improved embedding ab initio model potentials for embedded cluster calculations, J. Phys. Chem. A 113 (2009) 12454.

[122] A.S.P. Gomes, C.R. Jacob, Quantum-chemical embedding methods for treating local electronic excitations in complex chemical systems, Annu. Rep. Prog. Chem. Sect. C: Phys. Chem. 108 (2012) 222.

[123] J.D. Goodpaster, T.A. Barnes, F.R. Manby, T.F. Miller, 3Rd, Accurate and systematically improvable density functional theory embedding for correlated wavefunctions, J. Chem. Phys. 140 (2014) 18A507.

[124] T. Nguyen Lan, A.A. Kananenka, D. Zgid, Rigorous ab initio quantum embedding for quantum chemistry using Green's function theory: Screened interaction, nonlocal Self-Energy relaxation, orbital basis, and chemical accuracy, J. Chem. Theory Comput. 12 (2016) 4856.

[125] M. Dvorak, D. Golze, P. Rinke, Quantum embedding theory in the screened Coulomb interaction: Combining configuration interaction with BSE, Phys. Rev. Mater. 3 (2019) 070801.

[126] Z.-H. Cui, T. Zhu, G.K.-L. Chan, Efficient implementation of ab initio quantum embedding in periodic systems: Density matrix embedding theory, J. Chem. Theory Comput. 16 (2020) 119.

[127] P.V. Sriluckshmy, M. Nusspickel, E. Fertitta, G.H. Booth, Fully algebraic and self-consistent effective dynamics in a static quantum embedding, Phys. Rev. B 103 (2021) 085131.

[128] N. He, C. Li, F.A. Evangelista, Second-order active-space embedding theory, J. Chem. Theory Comput. (2022).

[129] G. Kotliar, S.Y. Savrasov, K. Haule, V.S. Oudovenko, O. Parcollet, C.A. Marianetti, Electronic structure calculations with dynamical mean-field theory, Rev. Modern Phys. 78 (2006) 865.

[130] K. Haule, Structural predictions for correlated electron materials using the functional dynamical mean field theory approach, J. Phys. Soc. Japan 87 (2018) 041005.

[131] K. Held, Electronic structure calculations using dynamical mean field theory, Adv. Phys. 56 (2007) 829.

[132] M. Bockstedte, F. Schütz, T. Garratt, V. Ivády, A. Gali, Ab initio description of highly correlated states in defects for realizing quantum bits, npj Quantum Mater. 3 (2018) 31.

[133] H. Ma, N. Sheng, M. Govoni, G. Galli, Quantum embedding theory for strongly correlated states in materials, J. Chem. Theory Comput. 17 (2021) 2116.

[134] H. Ma, M. Govoni, G. Galli, Quantum simulations of materials on near-term quantum computers, npj Comput. Mater. 6 (2020) 85.

[135] H. Ma, N. Sheng, M. Govoni, G. Galli, First-principles studies of strongly correlated states in defect spin qubits in diamond, Phys. Chem. Chem. Phys. 22 (2020) 25522.

[136] G. Barcza, V. Ivády, T. Szilvási, M. Voros, L. Veis, Á. Gali, O. Legeza, DMRG on top of plane-wave Kohn–Sham orbitals: A case study of defected boron nitride, J. Chem. Theory Comput. 17 (2021) 1143.

[137] W. Pfäffle, D. Antonov, J. Wrachtrup, G. Bester, Screened configuration interaction method for open-shell excited states applied to NV centers, Phys. Rev. B 104 (2021) 104105.

[138] L. Muechler, D.I. Badrtdinov, A. Hampel, J. Cano, M. Rösner, C.E. Dreyer, Quantum embedding methods for correlated excited states of point defects: Case studies and challenges, Phys. Rev. B 105 (2022) 235104.

[139] B.T.G. Lau, B. Busemeyer, T.C. Berkelbach, Optical properties of defects in solids via quantum embedding with good active space orbitals, J. Phys. Chem. C 128 (7) (2024) 2959–2966.

[140] J. Bhang, H. Ma, D. Yim, G. Galli, H. Seo, First-principles predictions of out-of-plane group IV and V dimers as high-symmetry, high-spin defects in hexagonal boron nitride, ACS Appl. Mater. Interfaces 13 (2021) 45768.

[141] R.P. Messmer, G.D. Watkins, Linear combination of atomic orbital-molecular orbital treatment of the deep defect level in a semiconductor: Nitrogen in diamond, Phys. Rev. Lett. 25 (1970) 656.

[142] S.G. Louie, M. Schlüter, J.R. Chelikowsky, M.L. Cohen, Self-consistent electronic states for reconstructed Si vacancy models, Phys. Rev. B 13 (1976) 1654.

[143] M. Mackoit-Sinkevičiene, M. Maciaszek, C.G. Van de Walle, A. Alkauskas, Carbon dimer defect as a source of the 4.1 eV luminescence in hexagonal boron nitride, Appl. Phys. Lett. 115 (2019) 212101.

[144] K. Era, F. Minami, T. Kuzuba, Fast luminescence from carbon-related defects of hexagonal boron nitride, J. Lumin. 24–25 (1981) 71.

[145] L. Museur, E. Feldbach, A. Kanaev, Defect-related photoluminescence of hexagonal boron nitride, Phys. Rev. B 78 (2008) 155204.

[146] X.Z. Du, J. Li, J.Y. Lin, H.X. Jiang, The origin of deep-level impurity transitions in hexagonal boron nitride, Appl. Phys. Lett. 106 (2015) 021110.

[147] J.F. Stanton, R.J. Bartlett, The equation of motion coupled-cluster method, a systematic biorthogonal approach to molecular excitation energies, transition probabilities, and excited state properties, J. Chem. Phys. 98 (1993) 7029.

[148] A.I. Krylov, Equation-of-motion coupled-cluster methods for open-shell and electronically excited species: The Hitchhiker's guide to Fock space, Annu. Rev. Phys. Chem. 59 (2008) 433.
[149] X. Wang, T.C. Berkelbach, Excitons in solids from periodic equation-of-motion coupled-cluster theory, J. Chem. Theory Comput. 16 (2020) 3095.
[150] X. Wang, T.C. Berkelbach, Absorption spectra of solids from periodic equation-of-motion coupled-cluster theory, J. Chem. Theory Comput. 17 (2021) 6387.
[151] N. Sheng, C. Vorwerk, M. Govoni, G. Galli, Green's function formulation of quantum defect embedding theory, J. Chem. Theory Comput. 18 (2022) 3512.
[152] K. Haule, Exact double counting in combining the dynamical mean field theory and the density functional theory, Phys. Rev. Lett. 115 (2015) 196403.
[153] A. Szabó, N. Ostlund, Modern Quantum Chemistry: Introduction to Advanced Electronic Structure Theory, Dover Publications, Mineola, NY, 1996.
[154] J.P. Perdew, K. Burke, M. Ernzerhof, Generalized gradient approximation made simple, Phys. Rev. Lett. 77 (1996) 3865.
[155] E.G.C.P. van Loon, M. Rösner, M.I. Katsnelson, T.O. Wehling, Random phase approximation for gapped systems: Role of vertex corrections and applicability of the constrained random phase approximation, Phys. Rev. B 104 (2021) 045134.
[156] X. Leng, F. Jin, M. Wei, Y. Ma, GW method and Bethe–Salpeter equation for calculating electronic excitations, Wiley Interdiscip. Rev.: Comput. Mol. Sci. 6 (2016) 532.
[157] B. Cunningham, M. Grüning, D. Pashov, M. van Schilfgaarde, QSGW: Quasiparticle self-consistent GW with ladder diagrams in W, Phys. Rev. B 108 (2023) 165104.
[158] Y. Jin, M. Govoni, G. Galli, Vibrationally resolved optical excitations of the nitrogen-vacancy center in diamond, npj Comput. Mater. 8 (2022) 238.
[159] Y. Chang, E.G.C.P. van Loon, B. Eskridge, B. Busemeyer, M.A. Morales, C.E. Dreyer, A.J. Millis, S. Zhang, T.O. Wehling, L.K. Wagner, M. Rösner, Downfolding from ab initio to interacting model hamiltonians: Comprehensive analysis and benchmarking of the DFT+cRPA approach, npj Comput. Mater. 10 (2024) 129.
[160] Z. Qiu, K. Vaklinova, P. Huang, M. Grzeszczyk, K. Watanabe, T. Taniguchi, K.S. Novoselov, J. Lu, M. Koperski, Atomic and electronic structure of defects in hBN: enhancing single-defect functionalities, ACS Nano 18 (2024) 24035.
[161] M. Grzeszczyk, K. Vaklinova, K. Watanabe, T. Taniguchi, K.S. Novoselov, M. Koperski, Electroluminescence from pure resonant states in hBN-based vertical tunneling junctions, Light: Sci. Appl. 13 (2024) 155.
[162] H.L. Stern, Q. Gu, J. Jarman, S. Eizagirre Barker, N. Mendelson, D. Chugh, S. Schott, H.H. Tan, H. Sirringhaus, I. Aharonovich, M. Atatüre, Room-temperature optically detected magnetic resonance of single defects in hexagonal boron nitride, Nature Commun. 13 (2022) 618.